HHS Public Access

Author manuscript

Sci Immunol. Author manuscript; available in PMC 2024 September 15.

Published in final edited form as:

Sci Immunol. 2023 September 15; 8(87): eadf6717. doi:10.1126/sciimmunol.adf6717.

Integrated BATF transcriptional network regulates suppressive intratumoral regulatory T cells

Feng Shan[1,2,3], **Anthony R. Cillo**[1,3], **Carly Cardello**[1,3], **Daniel Y. Yuan**[4], **Sheryl R. Kunning**[1,3], **Jian Cui**[1,3], **Caleb Lampenfeld**[1,3], **Asia M. Williams**[1,3], **Alexandra P. McDonough**[1,3], **Arjun Pennathur**[5,6], **James D. Luketich**[6], **John M. Kirkwood**[5,7], **Robert L. Ferris**[1,3,5], **Tullia C. Bruno**[1,3,5], **Creg J. Workman**[1,3], **Panayiotis V. Benos**[4,8], **Dario A. A. Vignali**[1,3,5,*]

[1]Department of Immunology, University of Pittsburgh School of Medicine, Pittsburgh, PA, USA.

[2]Integrative Systems Biology Program, University of Pittsburgh School of Medicine, Pittsburgh, PA, USA.

[3]Tumor Microenvironment Center, UPMC Hillman Cancer Center, Pittsburgh, PA, USA.

[4]Department of Computational and Systems Biology, University of Pittsburgh School of Medicine, Pittsburgh, PA, USA.

[5]Cancer Immunology and Immunotherapy Program, UPMC Hillman Cancer Center, Pittsburgh, PA, USA.

[6]Department of Cardiothoracic Surgery, University of Pittsburgh School of Medicine, Pittsburgh, PA, USA.

[7]Department of Medicine, Division of Hematology/Oncology, University of Pittsburgh School of Medicine, Pittsburgh, PA, USA.

[8]Department of Epidemiology, University of Florida, Gainesville, FL, USA.

Abstract

Human regulatory T cells (T_{regs}) are crucial regulators of tissue repair, autoimmune diseases, and cancer. However, it is challenging to inhibit the suppressive function of T_{regs} for cancer therapy without affecting immune homeostasis. Identifying pathways that may distinguish tumor-restricted T_{regs} is important, yet the transcriptional programs that control intratumoral T_{reg} gene expression, and that are distinct from T_{regs} in healthy tissues, remain largely unknown. We profiled

*Corresponding author. dvignali@pitt.edu.

Author contributions: D.A.A.V., C.J.W., P.V.B., and T.C.B. conceptualized the project. F.S., A.R.C., J.C., D.Y.Y., P.V.B., T.C.B., C.J.W., and D.A.A.V. developed the methodology used. F.S., C.C., D.Y.Y., S.R.K., C.L., A.M.W., and A.P.M. conducted investigation. F.S., D.Y.Y., and A.R.C. performed analyses and data visualization. A.P., J.D.L., J.M.K., and R.L.F. coordinated and obtained the clinical samples. D.A.A.V. acquired funding. A.R.C., T.C.B., P.V.B., C.J.W., and D.A.A.V. supervised the project. F.S., A.R.C., P.V.B., C.J.W., and D.A.A.V. wrote the paper.

Competing interests: D.A.A.V. is cofounder and stockholder of Novasenta, Potenza, Tizona, and Trishula; stockholder of Oncorus and Werewolf; has patents licensed and royalties from BMS and Novasenta; scientific advisory board member of Tizona, Werewolf, F-Star, Bicara, Apeximmune, and T7/Imreg Bio; is a consultant for BMS, Incyte, Regeneron, Ono Pharma, and Avidity Partners; and obtained research funding from BMS and Novasenta. T.C.B. receives research funding for Alkermes and Pfizer and is a consultant for Walking Fish Therapeutics, iTeos Therapeutics, and BeSpoke Therapeutics. A.R.C. is a consultant for AboundBio. A.P. is an investigator in a research grant to UPMC from Novasenta. J.D.L. is an investigator in a research grant to UPMC from Novasenta. All other authors declare that they have no competing interests.

single-cell transcriptomes of $CD4^+$ T cells in tumors and peripheral blood from patients with head and neck squamous cell carcinomas (HNSCC) and those in nontumor tonsil tissues and peripheral blood from healthy donors. We identified a subpopulation of activated T_{regs} expressing multiple tumor necrosis factor receptor (TNFR) genes ($TNFR^+$ T_{regs}) that is highly enriched in the tumor microenvironment (TME) compared with nontumor tissue and the periphery. $TNFR^+$ T_{regs} are associated with worse prognosis in HNSCC and across multiple solid tumor types. Mechanistically, the transcription factor BATF is a central component of a gene regulatory network that governs key aspects of $TNFR^+$ T_{regs}. CRISPR-Cas9–mediated *BATF* knockout in human activated T_{regs} in conjunction with bulk RNA sequencing, immunophenotyping, and in vitro functional assays corroborated the central role of BATF in limiting excessive activation and promoting the survival of human activated T_{regs}. Last, we identified a suite of surface molecules reflective of the BATF-driven transcriptional network on intratumoral T_{regs} in patients with HNSCC. These findings uncover a primary transcriptional regulator of highly suppressive intratumoral T_{regs}, highlighting potential opportunities for therapeutic intervention in cancer without affecting immune homeostasis.

INTRODUCTION

Regulatory T cells (T_{regs}) are essential for immune homeostasis. The development, maintenance, and function of T_{regs} depend on the transcription factor forkhead box protein 3 (FOXP3) (1). Individuals who lack FOXP3 expression develop immune dysregulation, polyendocrinopathy, enteropathy, and X-linked (IPEX) syndrome, a severe autoimmune lymphoproliferative disease that is fatal without bone marrow transplantation (2). However, in the tumor microenvironment (TME), tumor-infiltrating lymphocyte T_{regs} (herein referred to as $TILT_{regs}$) exert immune suppressive functions and subsequently inhibit immune-mediated tumor clearance, suggesting that immunotherapies should inhibit the suppressive function of TIL T_{regs} specifically to enhance antitumor immunity without affecting immune homeostasis (3, 4).

An elevated frequency of T_{regs} within a tumor is associated with an adverse prognosis across many cancers (5–9). The current methods of targeting T_{regs} in the clinic are direct T_{reg} depletion, targeting costimulatory or coinhibitory receptors, halting T_{reg} migration into the TME, and inducing T_{reg} fragility (10–14). However, immune-related adverse effects such as pneumonitis and colitis were seen in clinical studies of T_{reg}-targeted therapies (15–17). A major limitation underlying the autoimmune toxicity and limited efficacy observed with T_{reg} therapies in the clinic is an inability to target TIL T_{regs} selectively, with unwanted side effects resulting from inhibition of T_{regs} in the periphery or because the function of antitumor effector T cells is also impaired (12, 18).

We recently reported on the immune landscape of head and neck squamous cell carcinoma (HNSCC) (19). We found that TIL T_{regs} are phenotypically heterogeneous in the HNSCC TME and that only a small subset of TIL T_{regs} exhibited effector-like phenotypes. Identifying genes that are specific to TIL T_{reg}, but that are not present in peripheral T_{regs} nor effector T cells, is a strategy toward identifying molecules that could be potentially targeted for therapies aiming to modulate immunosuppressive T_{regs} in the TME specifically.

FOXP3, alone or in combination with the interleukin-2 (IL-2) receptor α-chain (IL2RA/CD25), is commonly used to detect TIL T_{regs} in tumor samples by immunohistochemistry and flow-based studies, but these approaches may be limited by the ability to incorporate an extended number of additional markers that allow identification of functionally active T_{regs} in the TME (20–22) or other distinctive gene expression signatures. In this study, we leveraged single-cell RNA sequencing (scRNA-seq) technology to provide a detailed view of the heterogeneity of T_{regs} in the TME by profiling $CD4^+$ T cells from tumors and peripheral blood mononuclear cells (PBMCs) taken from patients with HNSCC and comparing them with $CD4^+$ T cells isolated from inflamed tonsil tissues from patients with tonsilitis and from non-inflamed tonsil tissues from patients with sleep apnea and with healthy donor (HD) PBMCs. We identified a subset of activated TIL T_{regs} that expressed multiple tumor necrosis factor receptor (TNFR) member genes, including *TNFRSF4* (OX40), *TNFRSF9* (4–1BB), and *TNFRSF18* (GITR) (herein referred to as $TNFR^+$ T_{regs}). $TNFR^+$ T_{regs} were highly enriched in a variety of tumor types compared with nontumor tissues and are associated with worse prognosis across solid tumors. Using single-cell analysis approaches and graph-based modeling, we generated a comprehensive map of gene regulatory networks (GRNs) that govern TIL T_{reg} phenotypes. We found that basic leucine zipper ATF-like transcription factor (BATF), an activator protein-1 (AP-1) superfamily transcription factor (TF), is a central component of a GRN that controls the transcriptional signature of $TNFR^+$ T_{regs}. Knockout (KO) of *BATF* in cultured human activated T_{regs} with CRISPR-Cas9 in conjunction with immunophenotyping corroborated the central role of BATF in regulating activation and function of activated TIL T_{regs}. Bulk RNA sequencing (RNA-seq) and in vitro functional assays further interrogated the roles of BATF in human activated T_{regs}. The role of BATF in $TNFR^+$ T_{regs} was further corroborated in human T_{regs} under continuous T cell receptor (TCR) stimulation and hypoxic conditions (i.e., conditions that mimic the persistent antigenic stimulation and metabolic stress in the TME). Our analyses highlighted the regulatory roles of BATF with several surface markers differentially expressed on HNSCC TIL T_{regs}, including 4–1BB, OX40, GITR, CD74, CD96, and CD39. These findings revealed a distinct transcriptional signature of an intratumoral T_{reg} subpopulation that is associated with worse prognosis, identified distinct surface markers that define functionally suppressive T_{regs} within the TME, and provide insights into immunotherapeutic targets for the treatment of solid tumors.

RESULTS

HNSCC TIL T_{regs} have distinct transcriptional signatures compared with $CD4^+$ conventional T cells and peripheral T_{regs}

We recently reported on the immune landscape of HNSCC (19). To identify gene signatures and molecular pathways that are specific to human TIL T_{regs} over peripheral T_{regs} and effector T cells, $CD4^+$ conventional T cells (T_{conv}, $CD4^+CD25^{low}CD127^{high}$) and $CD4^+$ T_{regs} ($CD4^+CD25^{high}CD127^{low}$) were sorted from nontumor inflamed tonsils from patients with tonsilitis and HD PBMCs and profiled by scRNA-seq (fig. S1). We integrated these data with the raw sequencing data obtained from TIL $CD4^+$ T cells from the previously published HNSCC scRNA-seq dataset (19) as well as the sequencing data for $CD4^+$ T cells isolated from non-inflamed tonsils from patients with sleep apnea (Fig. 1A and fig. S2,

A and B). After filtering for quality control and data integration by Seurat v4 pipeline, we were able to obtain 51,195 $CD4^+$ T cells from 26 patients with HNSCC, 6 patients with tonsilitis, 5 patients with sleep apnea, and 10 HDs (data file S1, tab data S1) (23). After applying nonlinear dimension reduction using uniform manifold approximation and projection (UMAP) and Louvian graph–based clustering, $CD4^+$ T cells from various origins were partitioned into 19 clusters (fig. S2A). Most cells were grouped together on the basis of their cell types and cell origins, whereas several clusters retained both T_{conv} and T_{regs} from the same tissue source. Moreover, some clusters aggregated one of the cell types from different cell origins, suggesting that there were tissue-intrinsic signatures and phenotypic overlap between $CD4^+$ T cells (Fig. 1, B and C, and fig. S2B). For instance, both T_{conv} and T_{regs} from HD PBMCs expressed high levels of *TCF7* and *S1PR1*, and T_{conv} and T_{regs} from both inflamed and non-inflamed tonsils were enriched in *FOS* and *DUSP1* (fig. S2C and data file S1, tab data S1). We detected relatively higher levels of *IL7R* and *TCF7* expression in tonsil T_{conv} from patients with sleep apnea compared with those from patients with tonsilitis. In addition, higher expression of *CTLA4*, *TNFRSF1B*, and *IFITM1* in tonsil T_{conv} from patients with tonsilitis, compared with the non-inflamed controls, suggested a more inflamed signature of $CD4^+$ T_{conv} in patients with tonsilitis (fig. S3, A to E). This inflamed tissue signature was further confirmed by enrichment of pathways involving CD28 costimulation signaling, nuclear factor κB (NF-κB) signaling, and IL-12 family signaling in $CD4^+$ T_{conv} from patients with tonsilitis (fig. S3, F to I). However, although we detected the expression of *TNFRSF4* and *TNFRSF18* in HNSCC PBMC T_{regs}, they were increased in HNSCC TIL T_{regs} compared with HNSCC PBMC T_{regs} and nontumor tonsil tissue T_{regs} (fig. S2C).

To characterize TIL T_{reg}-specific signatures further, we examined differentially expressed genes and published gene sets in HNSCC TIL T_{regs} compared with T_{regs} in nontumor tissue, in peripheral blood from patients with HNSCC and T_{conv} from all sites. In particular, HNSCC TIL T_{regs} expressed *ICOS*; *CD27*; and TNFR members *TNFRSF4*, *TNFRSF9* (the gene encoding 4–1BB), and *TNFRSF18*, which reflected a specific activated T_{reg} phenotype. These TIL T_{regs} were also enriched for a gene set associated with noncanonical TNFR2-NF-κB pathway (Fig. 1, D and E and data file S1, tab data S2) (21, 24). In addition to up-regulation of IL-10 signaling, we also detected selective expression of *CTLA4*, *TIGIT*, and *ENTPD1* (gene for CD39) in HNSCC TIL T_{regs}, highlighting a potentially more suppressive phenotype of T_{regs} in the HNSCC TME compared with tissue T_{regs} and peripheral T_{regs} (Fig. 1, D and E). Type I/II interferon (IFN) response signatures, including *ISG15*, *IFI6*, *IFI16* (Fig. 1D), and a gene set associated with response to IFN-γ (Fig. 1E) were observed in HNSCC TILT_{regs}, implying that T_{regs} undergo functional specialization after activation in the TME. Through cross-checking all differentially expressed genes in HNSCC TIL T_{regs} with a published human TF database (25), we identified six TFs highly expressed in HNSCC TIL T_{regs}, including *BATF*, *CREM*, *CARD16*, *SOX4*, *IRF7*, and *STAT1* (Fig. 1D). By contrast, HD PBMC T_{regs} were characterized by naïve T_{reg} signatures including high levels of *TCF7* and *S1PR1* (Fig. 1D) as well as gene sets associated with EZH2, FOXP3, early differentiation, and naïve T cell pathways (Fig. 1E and fig. S2C). Tonsil tissue T_{regs} exhibited an early activation phenotype by up-regulating *FOS* and gene sets associated with histone modifications, chromatin organization, and mitogen-activated protein kinase

(MAPK) activation (Fig. 1E and fig. S2C). In addition, a heat shock response gene set and associated genes were highly enriched in T_{regs} from tonsils (Fig. 1E and fig. S2C). Although we detected mRNA expression of *BATF* in tonsil T_{regs} from patients with tonsilitis, it was increased in HNSCC TIL T_{regs} compared with tonsil tissue T_{regs} from patients with tonsilitis or sleep apnea (fig. S3J). We observed similar gene expression profiles in nontumor tonsil T_{regs} from patients with sleep apnea or tonsilitis and distinct from those in the HNSCC TME, suggesting a specific gene expression signature of TIL T_{regs} compared with inflamed and non-inflamed tissues (fig. S3, K to P). These analyses provided an overview of expression signatures differentially enriched in HNSCC TIL T_{regs} versus T_{regs} in nontumor tissues and the periphery and the distinct transcriptional signatures from T_{conv} from various tissue sites.

TNFR$^+$ T_{regs} are a distinct differentiation state and correlate with worse prognosis in patients with HNSCC

To characterize the heterogeneity of T_{regs} within the HNSCC TME and understand the context-dependent mechanisms modulating different T_{reg} subsets in the HNSCC TME, we refined the T_{reg} analysis by partitioning them into 13 subclusters (Fig. 2A; fig. S4, A and B; and data file S1, tab data S3). We also performed pseudotemporal modeling of differentiation using RNA velocity (26). The inferred pseudotemporal ordering indicated a differentiation trajectory across T_{reg} clusters (Fig. 2B and fig. S4C). On the basis of the pseudotime trajectory, canonical marker genes and gene sets that associated with distinct T cell state transitions defined 13 clusters, characterized as naïve/memory T_{regs} (clusters 1 to 5), early activated T_{regs} (clusters 6 to 8), TNFR$^+$ T_{regs} (clusters 9 to 12), and IFN$^+$ T_{regs} (cluster 13) (Fig. 2, B to D, and fig. S4, C and D). For instance, T_{reg} clusters 1 to 5 were identified as naïve/memory T_{regs} by up-regulation of *SELL* (gene encoding L-selectin), *CCR7*, and *TCF7* as well as gene sets associated with ribosome and naïve T cell signatures (Fig. 2D and fig. S4D). In addition to enhanced expression of *FOS*, *JUN*, and *BCL2*, gene sets associated with T cell activation including phosphorylation of β-actin, activation of AP-1 family signaling, and MAPK3/ERK activation were highly enriched in T_{reg} clusters 6 to 8. We found two T_{reg} subsets that are highly activated and characterized by the up-regulation of gene sets associated with coinhibitory receptor programmed cell death protein 1 (PD-1) and cytotoxic T-lymphocyte-associated protein 4 (CTLA-4) signaling and TNFRSF-induced noncanonical NF-κB pathway. These signatures were confirmed by expression levels of TNFR super family members [*TNFRSF4*, *TNFRSF18*, and *TNFRSF1B* (gene encoding TNFR2)] and coinhibitory/stimulatory receptors [*ICOS*, *CTLA4*, and *PDCD1* (gene encoding PD-1)] (Fig. 2D and fig. S4D). However, genes and gene sets associated with IFN-stimulated responses (*IFIT3*, *ISG15*, and *IFI6*) were exclusively enriched in cluster 13 (IFN$^+$ T_{regs}) (Fig. 2D and fig. S4D). In addition, cells within cluster 13 highly expressed genes associated with T helper cell type 1 (T_H1) phenotype, including *TBX21* (gene encoding T-bet), *CCL4*, *CCL5*, and *IFNG* (gene encoding IFN-γ), suggesting a specialized function of T_{regs} for T_H1-related and antiviral immune responses (fig. S4D) (27–29). We also detected augmented expression of *CD39* and *CD27* in T_{reg} clusters 9 to 12 (TNFR$^+$ T_{regs}), which highlighted different programs regulating activated T_{reg} function in the TME. A pseudotemporal ordering by RNA velocity further revealed that the TNFR$^+$ T_{regs} and IFN$^+$ T_{regs} were the most terminally differentiated T_{reg} subpopulations (fig. S4E).

Most cells identified as TNFR$^+$ T_{regs} and IFN$^+$ T_{regs} were predominantly enriched in the HNSCC TME, whereas nontumor tonsil tissues were enriched in naïve/memory and early activated T_{regs}, demonstrating both tumor-specific and overlapping phenotypes of T_{regs} in the TME versus nontumor tissues (fig. S4F).

To determine whether the enrichment of T_{reg} subpopulations was related to survival outcomes of patients, we performed survival analysis using clinical data and bulk RNA-seq expression data from the Cancer Genome Atlas (TCGA). We scored each patient for the enrichment of T_{reg} signatures derived from HNSCC scRNA-seq data and used the enrichment score as a reference profile to impute T_{reg} enrichment in bulk RNA-seq datasets by CIBERSORTx (30). Gene sets representing T_{reg} enrichment were derived from the top 200 differentially expressed genes in each T_{reg} subpopulation. We found that high enrichment of TNFR$^+$ T_{regs} in patients with HNSCC was associated with worse progression-free survival (PFS), suggesting that this TIL T_{reg} subpopulation suppresses antitumor immunity in HNSCC (Fig. 2E). By contrast, the enrichment of early activated T_{regs} or IFN$^+$ T_{regs} did not show association with survival (Fig. 2E). Although the enrichment of naïve/memory T_{regs} was also associated with poorer survival of patients, these naïve/memory T_{reg} signatures were not tumor specific because they were observed in the periphery and nontumor tissues (Fig. 2E and fig. S4F). The frequency of TNFR$^+$ T_{regs} was not correlated with CD8$^+$ T cells, CD4$^+$ T_{conv}, or natural killer (NK) cells in the HNSCC TME (Fig. 2F). In addition, the enrichment of each T_{reg} subpopulation did not show correlation with each other (fig. S5A). Fisher's exact test indicated that there was no association between the enrichment of TNFR$^+$ T_{regs} with overall T_{reg} infiltration, patients' clinical stage, or human papillomavirus (HPV) status of patients with HNSCC (fig. S5B). To assess whether the TNFR$^+$ T_{reg} signature used in the survival association analysis is shared by other cell types, we calculated the enrichment score for the TNFR$^+$ T_{reg} signature in other immune cell types present in the HNSCC TME. Minimal enrichment scores were identified in other immune cell types, further suggesting that the association of TNFR$^+$ T_{regs} and survival outcomes of patients with HNSCC was not confounded by the gene signatures of other T_{reg} subpopulations or other cell types. (Fig. 2G). After correcting the clinical stage, overall T_{reg} infiltration, HPV status of patients, tumor infiltrations of CD8$^+$ T cells, CD4$^+$ T_{conv} or NK cells as covariates, the association between worse PFS and high TNFR$^+$ T_{reg} enrichment remained in a multiple variable survival analysis, indicating that the association of TNFR$^+$ T_{regs} and patient survival outcomes was not confounded by tumor infiltration of other cell types or clinical factors (Fig. 2H).

GRN inference revealed critical transcriptional circuit controlling TNFR$^+$ T_{reg} subpopulation

Cell state transitions during T cell activation are governed by TFs and their associated cofactors, which work together to regulate gene expression and cell function. To determine transcriptional regulators critical to TIL T_{regs} at each cell state, we systematically assessed the genes that are likely to be governed by TFs in each T_{reg} subpopulation by applying SCENIC (31) to infer TF activity and downstream target genes (Fig. 3A and data file S1, tab data S4). Naïve/memory T_{regs} were highly enriched with well-known TFs mediating T cell homeostasis including *KLF2* and *FOXP1* (32, 33), whereas regulons governed by *EGR1*

and AP-1 family TFs (*FOSB* and *FOS)*, known as important regulators of T cell activation and early response to TCR engagement, were detected in early activated T_{regs} (34). In activated T_{reg} subsets, enrichment of regulons *IRF2*, *TBX21*, and *EOMES* was increased in IFN^+ T_{regs}, reflecting the specialized T_{reg} function for helper T cell responses (28, 35, 36). Regulons governed by *BATF*, *EPAS1*, and noncanonical NF-κB pathway genes including *NFKB2*, *RELB*, and *BCL3* showed enhanced activities in $TNFR^+$ T_{regs} (Fig. 3A). NF-κB family genes are well-known for regulating T_{reg} function and development (37–39). *EPAS1*, which encodes the hypoxia-inducible factor 2A, has been recently described for its role in moderating the development and function of T_{regs} (40, 41). Although BATF was identified as a driver of key regulons in T_{regs}, it is unknown what transcriptional regulation(s) or T_{reg} subpopulations are governed by expression of genes controlled by this TF.

Limitations of scRNA-seq technologies, such as dropouts, stochastic variation of gene expression at the single-cell level, and the relatively low expression of some TFs, can hamper the detection of TFs orchestrating cellular identity and function. Despite the minimal gene expression of *NFKB2*, *RELB*, and *BCL3,* regulons governed by these TFs were enriched with several TNFR members and showed differential enrichment in $TNFR^+$ T_{regs} (fig. S6, A and B). Moreover, we found that multiple downstream target genes were shared by top enriched regulons in each T_{reg} subpopulation, suggesting a synergistic regulation of TFs controlling T_{reg} identity, activation, and function in the TME. We integrated the top five regulons into combined GRNs and discovered distinct signaling pathways that are specific to each T_{reg} subpopulation (figs. S7 and S8, A to D). Reactome pathway analysis showed that forkhead box class O (FOXO)–mediated signaling and RUNX3-mediated signaling were enriched in the GRN identified in naïve/memory T_{regs} (fig. S8A). In early activated T_{regs}, cell cycle checkpoint, cellular response to stimuli, and NOTCH-mediated signaling in the GRN represented the pathways vital for T_{reg} proliferation and activation (fig. S8B). In addition to TNFR members mediating noncanonical NF-κB pathway, we also observed that the GRN from $TNFR^+$ T_{regs} are highly involved in cell apoptosis and IL-4/IL-13 and IL-10 signaling pathways, and the GRN from IFN^+ T_{regs} plays important roles in type I/II IFN responses, cell death, and antigen presentation signaling (fig. S8, C and D).

We next used directed mixed graphical modeling (MGM) and fast causal inference-Max (FCI-MAX) (42) to define the central regulatory circuit controlling the GRN of $TNFR^+$ T_{regs}. Genes with near-zero variance and low overall nonzero values were filtered out, and normalized gene expression data from $TNFR^+$ T_{reg} were used as input. All downstream targets of the top five enriched regulons in $TNFR^+$ T_{regs} were used to construct an undirected network by using MGM. The central regulatory network was imputed using FCI-MAX by connecting the key transcriptional regulators and downstream targets within the undirected network. We found that *BATF* is central to the $TNFR^+$ T_{reg} GRN by having the most connections compared with other genes (Fig. 3B). In addition, *BATF* was predicted to regulate multiple key signatures of HNSCC TIL T_{regs} as previously defined. For instance, *BATF* is directly linked to costimulatory/inhibitory receptors *TNFRSF4*, *TNFRSF9*, *TNFRSF1B*, *CD27*, *ICOS*, *IL2RA*, and *CTLA4*, which have been shown to be important in TIL T_{reg} activation and function. Furthermore, we found that the chemokine receptor *CXCR6* and T cell apoptosis signaling molecules *CFLAR* (gene encoding c-FLIP) and *PIM3* were directly connected to *BATF* in the regulatory circuit, demonstrating a

potential role for *BATF* in controlling TIL T_{reg} migration and survival (Fig. 3B) (43–45). Together, we identified that $TNFR^+$ T_{regs} were a distinct differentiation state compared with other T_{reg} subpopulations, showed distinct gene expression signatures, and that this activated subpopulation was associated with worse prognosis of patients with HNSCC. By constructing the regulatory networks from scRNA-seq, we identified specific GRNs that govern T_{reg} phenotypes in HNSCC across cell states and inferred a transcriptional circuit centered around *BATF* that is central to $TNFR^+$ T_{regs} in the TME.

$TNFR^+$ T_{regs} are enriched in multiple solid tumor types and regulated by similar transcriptional programs

To validate whether this $TNFR^+$ T_{reg} subpopulation is distinct to the HNSCC TME, we isolated T_{regs} from matched tumors and blood from four patients with non–small cell lung cancer (NSCLC), one patient with small cell lung cancer (SCLC), and four patients with melanoma (Fig. 4A and fig. S9A). Unbiased clustering revealed six T_{reg} clusters that were evenly mixed with T_{regs} from melanoma and lung cancer and that exhibited distinct enrichment from T_{regs} from TILs or peripheral blood (Fig. 4B and fig. S9B). Cell states of T_{regs} were characterized by using RNAvelocity to evaluate differentiation and identifying genes associated with each T_{reg} subpopulations (Fig. 4C and fig. S9, C and D). We found that clusters 4 to 6 were predominantly enriched with TIL T_{regs} and expressed T_{reg} activation–related immune markers, including *ICOS*, *CD27*, and *TIGIT* (fig. S9, E to G). Cluster 6 was highly enriched with $TNFR^+$ T_{reg} signatures identified in the HNSCC TME, whereas cells in cluster 5 expressed IFN^+ T_{reg} signatures (Fig. 4, D and E, and fig. S9, G to N). Next, we quantified the activity for each regulon derived from HNSCC $TNFR^+$ T_{regs} in the TIL T_{reg} analyses in this dataset (46). Consistent with our analysis of HNSCC T_{regs}, the regulon governed by *BATF* was up-regulated in $TNFR^+$ T_{regs} (cluster 6) in the tumors from patients with lung cancer and melanoma (Fig. 4F).

In addition, we isolated T_{regs} from a previously published dataset (47) involving breast cancer, colorectal cancer, lung cancer, and ovarian cancer and interrogated their gene expression signatures and pseudotime trajectory (Fig. 4, G and H, and fig. S10A). We found that T_{regs} in clusters 6 and 7 expressed TNFR members and *BATF*, in agreement with our analyses of other tumor types (Fig. 4, I to K, and fig. S10B). By contrast, TIL T_{reg} cluster 5 expressed high levels of IFN-stimulated genes (*ISF15*, *IFI16*, and *IFI44L*) as well as markers associated with T cell activation (*ICOS* and *CD69*) (Fig. 4K and fig. S10B). Consistent with our previous analyses, we observed that regulons governed by *BATF*, *NFKB2*, *BCL3*, *RELB*, and *EPAS1* showed the highest activity scores in $TNFR^+$ T_{regs} (Fig. 4L).

To investigate whether $TNFR^+$ T_{regs} are present in both squamous cell carcinoma (SCC) and non-SCC histology types, we grouped TIL T_{regs} by histological types of cancers (fig. S11A). We found that $TNFR^+$ T_{regs} were enriched in patients with adenocarcinoma or SCC (fig. S11B). In addition to a similar expression level of *BATF*, we also observed comparable BATF regulon enrichment and $TNFR^+$ T_{reg} enrichment scores in $TNFR^+$ T_{regs} from patients with adenocarcinoma or SCC (fig. S11, C and D). The expression of *BATF*, BATF regulon activity, and $TNFR^+$ T_{reg} enrichment scores were also further confirmed in $TNFR^+$ T_{regs} in patients with invasive ductal carcinoma or large cell carcinoma, suggesting that $TNFR^+$ T_{regs}

and the associated BATF regulatory network were not cancer subtype specific (fig. S11, E to G).

The enrichment of TNFR$^+$ T$_{regs}$ was correlated with worse PFS for patients with NSCLC and melanoma (Fig. 4M). By acquiring data from the Genotype-Tissue Expression Project (GTEx) and imputing the enrichment of T$_{reg}$ subpopulations within normal tissues, we found higher enrichment of TNFR$^+$ T$_{regs}$ in solid tumors compared with normal lung and normal skin (sun exposed) (Fig. 4N). These observations show that at least a subset of activated TIL T$_{regs}$ have a distinct transcriptional signature versus T$_{regs}$ present in normal tissues. The transcriptional programs modulating TNFR$^+$ T$_{reg}$ function revealed by GRN construction are not specific to the HNSCC TME but are also present in other cancer types. These findings confirm that TNFR$^+$ T$_{regs}$ are enriched in multiple cancers compared with normal tissues, inferring an immunosuppressive role in the TME.

BATF functions as a transcriptional nexus of human activated T$_{regs}$

Our system approach can identify key TFs that modulate cellular functions in TIL T$_{regs}$, but it is crucial to experimentally validate the inferred GRNs. To investigate the impact of BATF on the expression of regulon members in the TNFR$^+$ T$_{regs}$ and validate our network prediction from scRNA-seq analyses, we used a CRISPR-Cas9 ribonucleoprotein (CRISPR RNP) KO approach that was developed to specifically target cultured primary human T$_{regs}$ (fig. S12, A and B) (48). Given the challenge of isolating an adequate number of activated TIL T$_{regs}$ from patients with cancer and the limitations of current CRISPR-Cas9 editing technology for targeting low numbers of human T cells, we used ex vivo expanded human primary T$_{regs}$ isolated from umbilical cord blood as a surrogate to interrogate the impact of *BATF* deletion at the transcriptional, protein, and functional levels. CRISPR RNPs targeting *BATF* or scrambled control RNPs (functional RNPs loaded with scrambled guide RNAs) were electroporated into expanded human T$_{regs}$. After a 3-day TCR stimulation post-electroporation, the expression levels of *BATF*, surface and intracellular proteins, and cytokines were evaluated by multiparameter flow cytometry. A robust reduction in the BATF protein level was observed in *BATF* KO activated T$_{regs}$ compared with the scrambled control (Fig. 5, A and B). These data suggested that the CRISPR RNP KO approach successfully altered BATF RNA and protein levels and allowed us to examine the effects of *BATF* disruption in human primary activated T$_{regs}$.

To dissect the phenotypic and functional effects of *BATF* in human activated T$_{regs}$, we performed RNA-seq of *BATF* KO activated T$_{regs}$ and scrambled controls from six cord blood samples. Results from principal components (PC) analysis revealed that PC1 stratified T$_{regs}$ by *BATF* KO versus scramble control (Fig. 5C and fig. S12C). Genes associated with T cell migration (*CCR7*, *CXCR6*, and *S1PR1*), cytokines (*IFNG*, *IL10*, and *IL13*), and cytokine receptors (*IL23R* and *IL1RL1*) were the strongest drivers of PC1 observed between *BATF* KO activated T$_{regs}$ and the scrambled control, suggesting an important role of *BATF* in activated T$_{reg}$ trafficking and function (Fig. 5D). To further characterize the functions of *BATF* in HNSCC intratumoral TNFR$^+$ T$_{regs}$, we evaluated all differentially expressed genes of TNFR$^+$ T$_{regs}$ from the HNSCC scRNA-seq dataset and interrogated their transcriptional changes in *BATF* KO activated T$_{regs}$. In addition to the reduction of

CXCR6 and *CCR7*, we observed gene sets associated with T_{reg} migration down-regulated in *BATF* KO activated T_{regs} compared with scrambled control, including chemokine receptors signaling during T cell polarization and NTN1 signaling (Fig. 5E). NTN1 encodes *Netrin-1*, which is a neuronal guidance molecule that was shown to increase T_{reg} infiltration to lung tissues of mice with lung ischemia-reperfusion (49). These data suggested a potential role of BATF in T_{reg} infiltration into the TME. We also detected a complex impact of *BATF* deletion in human activated T_{regs}, including up-regulation of gene sets associated with signaling of SMAD2/3, WNT signaling, and the TNFRSF/NF-κB pathway, as well as the down-regulation of gene sets associated with special AT-rich sequence-binding protein1 (SATB1) and MAPK signaling pathways (Fig. 5E). Moreover, *BATF* KO activated T_{regs} exhibited an increase in TCR signaling–related genes (*HLA-DQA1* and *CD82*) and NF-κB signaling–related gene *TRAF1*, which further indicated the important role of *BATF* in controlling T_{reg} activation (Fig. 5F). In addition to a reduction of *BCL2* expression in *BATF* KO activated T_{regs}, we found gene sets associated with apoptosis highly up-regulated in *BATF* KO activated T_{regs} along with increased expression of *BID*, an antagonist of *BCL2*, suggesting that BATF is essential for activated T_{reg} survival (Fig. 5, E to G). Together, by interrogating the impact of BATF disruption on genes that are selectively modulated in intratumoral $TNFR^+$ T_{regs}, we found that BATF is a critical regulator mediating multiple signaling pathways in human activated T_{regs}. These data suggested that BATF functions to limit excessive activation of human activated T_{regs} and promotes activated T_{reg} survival and trafficking.

BATF regulates the suppressive function of human activated T_{regs}

Given these observations, we hypothesized that BATF might also modulate the suppressive function of human activated T_{regs}. Although the protein level of FOXP3 and CD25 remained unchanged with *BATF* deletion, we observed an increase of suppressive function of *BATF* KO activated T_{regs}, demonstrating that human activated T_{regs} maintained their identity with *BATF* deletion and that the impact on T_{reg}-suppressive function is independent of *FOXP3* signaling (Fig. 6, A to C). Consistent with these results, *BATF* KO T_{regs} exhibited an increased activated phenotype exemplified by increased expressions and proportions of cells expressing the costimulatory receptors such as ICOS, OX40, and 4–1BB on T_{regs} (Fig. 6, D to F). We also detected an increased proportion of human activated T_{regs} expressing coinhibitory receptor LAG3, inhibitory cytokine IL-35 subunit EBI3, and IL-10, highlighting the increased suppression after *BATF* deletion in activated T_{regs} (Fig. 6, G to I, and fig. S12D). The number of human activated T_{regs} expressing NRP1 and the per-cell expression level of $NRP1^+$ T_{regs} were enhanced by *BATF* ablation, indicating an important role for *BATF* in regulating T_{reg} stability (Fig. 6J and fig. S12E) (50). These results were consistent with their transcript levels in *BATF* KO T_{regs} from bulk RNA-seq (fig. S12F). Together, these findings revealed a critical role of BATF in modulating the stability of activated T_{regs} and functioning independently of FOXP3 to control activated T_{reg}-suppressive function.

T_{regs} given continuous TCR stimulation under hypoxia mirror intratumoral $TNFR^+$ T_{regs} and are regulated by BATF

A recent study has shown that continuous TCR stimulation under hypoxia (low oxygen levels) resulted in severe T cell dysfunction consistent with a T cell exhaustion phenotype (51). We then adapted this in vitro system to mimic the persistent antigenic stimulation and metabolic stress in the TME and interrogate the role of BATF in T_{regs} under these conditions. Briefly, T_{regs} were isolated from cord blood and stimulated with magnetic beads coated with anti-CD3/anti-CD28 for 24 hours in the presence of IL-2, then washed, and split into four conditions (fig. S13A). Cells were expanded with IL-2 only ("acute" TCR stimulation) or cocultured with anti-CD3/anti-CD28–coated beads and IL-2 ("continuous" TCR stimulation). These T_{regs} under acute or continuous TCR activation were cultured in either normoxic (18.6% O_2) or hypoxic (1.5% O_2) gas atmosphere conditions for 10 days. We observed an increase in BATF in T_{regs} after continuous TCR stimulation under hypoxia compared with T_{regs} exposed to continuous TCR stimulation or hypoxia alone (Fig. 7, A and B). In addition, we detected a higher frequency of TNFR family members (4–1BB and GITR) on T_{regs} given continuous TCR stimulation under hypoxia compared with other conditions (Fig. 7, C and D). We also observed that LAG-3 and PD-1 were highly expressed on T_{regs} given continuous TCR stimulation under hypoxia, consistent with the phenotype of $TNFR^+$ T_{reg} in our scRNA-seq analyses above (Fig. 7, E and F, and fig. S4D). In addition, we also detected a substantive increase in molecules associated with T cell exhaustion (TIM-3 and TOX) in T_{regs} given continuous TCR stimulation under hypoxia (Fig. 7, G and H). Although KI67 was increased in T_{regs} given continuous TCR stimulation, there was no difference between normoxic and hypoxic conditions (Fig. 7I). Together, human T_{regs} cultured in this in vitro system mirrored many of the features of intratumoral $TNFR^+$ T_{regs}, suggesting that this system provides an opportunity to interrogate the role of BATF in $TNFR^+$ T_{regs}.

To further assess whether BATF serves as a nexus for modulating $TNFR^+$ T_{regs}, *BATF* deletion was conducted by CRISPR RNP KO in human T_{regs} with continuous TCR stimulation under hypoxia at day 10 (fig. S13, A and B). After 48-hour repeated TCR stimulation in hypoxia post-electroporation, a substantive reduction of BATF was observed after CRISPR targeting compared with the scrambled control (Fig. 7, J and K). Consistent with our previous analyses, we detected increased expression of 4–1BB, GITR, and OX40 in *BATF* KO T_{regs}, further confirming the important roles of BATF in modulating the activation of $TNFR^+$ T_{regs} (Figs. 6, F and G, and 7, L to N).

BATF regulates the cell surface phenotype of $TNFR^+$ T_{regs}

TNFR member genes have been reported in TIL T_{regs} and are associated with a late differentiated state found in various cancer types (19, 52). Although several agonistic antibodies of TNFR members are under development to target T_{regs} in the TME, these therapeutic targets may also modulate circulating T_{regs} and cause immune-relative adverse events (12, 53, 54). Identifying additional surface markers expressed on $TNFR^+$ T_{regs} is thus warranted to aid future development of immunotherapies with activity specifically in the TME. We were able to detect multiple genes that were differentially expressed on $TNFR^+$ T_{regs} compared with other T_{reg} subpopulations, including *CD96*, *CD39*, and *CD74* and

TNFR super family genes (*TNFRSF9* and *TNFRSF4*) (Fig. 8A). We observed reduction of CD96 and CD39 in *BATF* KO activated T_{regs} and a higher frequency of GITR, CD83, and CD74 (Fig. 8B). The differential expression (DE) changes of CD39 and CD83 were further confirmed in *BATF* KO T_{regs} with continuous TCR stimulation in hypoxia (fig. S13, C and D). We next sought to evaluate whether these cell surface markers were reflective of the BATF-driven $TNFR^+$ T_{regs} in patients with cancer. To assess this, we interrogated PBMCs and TILs from six patients with HNSCC and found higher frequency and increased expression of BATF, OX40, 4–1BB, and GITR on TIL T_{regs} compared with T_{regs} in HNSCC PBMCs and HD PBMCs (fig. S14A). The preferential expression of BATF, OX40, 4–1BB, and GITR in HNSCC TIL T_{regs} remained when comparing with T_{regs} in the periphery as well as $CD8^+$ T cells and $CD4^+$ T_{conv} in the HNSCC TME (Fig. 8, C to G, and fig. S14, B to D). In addition, OX40, 4–1BB, and GITR were coexpressed with BATF in HNSCC TIL T_{regs}, which supported the notion that BATF modulated the identity and activation of $TNFR^+$ T_{regs} (Fig. 8, E to G, and fig. S14, B to D). We also observed that CD96, CD39, and CD74 were highly expressed in HNSCC TIL T_{regs} compared with peripheral T_{regs}, $CD8^+$ T cells and $CD4^+$ T_{conv} in the HNSCC TME and showed a coexpression signature with BATF in HNSCC TIL T_{regs} (Fig. 8, H to J, and fig. S14, E to G). These findings revealed a distinct cell surface phenotype of activated T_{regs} regulated by BATF in the HNSCC TME, which provides additional opportunities for therapeutic intervention targeting intratumoral functionally suppressive T_{regs}.

DISCUSSION

T_{regs} are important regulators of immune homeostasis and tissue repair but suppress antitumor immunity (1, 3, 10, 29, 55–58). A previous study revealed conserved effector T_{reg} phenotypes that are shared between normal tissues and melanoma (45). In contrast, we found a T_{reg} subpopulation that was restricted to the TME and that expressed high levels of genes encoding TNFR family member. This T_{reg} subpopulation was associated with worse survival in HNSCC, melanoma, and lung cancer. These $TNFR^+$ T_{regs} exhibited a highly suppressive phenotype compared with all other T_{reg} subpopulations and had a distinct transcriptional program compared with all T_{conv}. By further characterizing the heterogeneity of T_{regs} within the tumor, our results revealed the diversity of cell states that TIL T_{regs} can acquire, highlighting the urgency of understanding the cell-intrinsic signaling that modulates the phenotypic state of functionally suppressive T_{regs}. Our work provides a comprehensive view of gene networks coordinating signaling mechanisms essential for key T_{reg} phenotypes at each state.

The reconstruction of GRN by SCENIC and directed MGM allowed us to identify critical TFs and target genes modulating the activation, migration, and function of T_{regs} that are functionally suppressive in HNSCC TME, specifically intratumoral $TNFR^+$ T_{regs}. Validation using an additional dataset that included T_{regs} from lung cancer and melanoma as well as an independent dataset that included T_{regs} from breast cancer, colorectal cancer, lung cancer, and ovarian cancer (47) further confirmed the presence of intratumoral $TNFR^+$ T_{regs}. These findings underscore the importance of these intratumoral $TNFR^+$ T_{regs} and the GRN that governs this cell state across solid tumors. The conservation of phenotypes and the GRN governing them across distinct solid tumor types suggests that modulation of T_{regs} could

be broadly used to therapeutically enhance antitumor immunity in a wide variety of tumor types.

BATF showed the highest gene expression level among all TFs in TIL T_{regs} and was enriched in $TNFR^+$ T_{regs}. Although previous studies supported an accumulation of BATF expression during T_{reg} activation within the TME in several cancers (47, 59), the role for BATF in controlling the function and activation of differentiated and activated T_{regs} in the TME was unclear. BATF is one of the AP-1 family members that has shown important roles in many T cell lineages (60). Within the $CD4^+$ T cell lineage, BATF is required for the differentiation of IL-17–producing helper T cells and plays an important role in the development of follicular helper T cells (61, 62). Furthermore, BATF is required for differentiation of effector $CD8^+$ T cells (60). Studies of $CD8^+$ T cells suggest that BATF positively regulates lineage-specific TFs including *TBX21* and *PRDM1* during effector cell differentiation while negatively regulating downstream effector molecules such as IFN-γ, perforin, and granzyme B (60). Conversely, increased expression of BATF in exhausted $CD8^+$ T cells suppresses their effector function (63). Such counterintuitive roles of BATF indicate distinct regulatory functions at different T cell states and cell subtypes. In T_{regs}, BATF has been found to regulate differentiation and accumulation of tissue T_{regs} and modulate the development and maintenance of adipose tissue resident T_{regs} in murine *Foxp3*-mutant and *Batf*-deficient mouse models (64, 65). A recent study suggested that BATF epigenetically promotes activation of TIL T_{regs}, and BATF deficiency in T_{regs} resulted in inhibited tumor growth in murine models (58). Consistent with previous studies, we found that BATF and the BATF integrated network play important roles in controlling key gene signatures that regulate the differentiation and activation of TIL T_{regs}. However, conditional deletion in *Batf*-deficient mice occurs before T_{reg} differentiation, complicating the evaluation of transcriptional and functional changes in activated intratumoral T_{regs}. We hypothesized that BATF exhibits distinct roles at different T_{reg} states and plays an especially important role in highly activated T_{regs}. Understanding the function of BATF in activated TIL T_{regs} is necessary to uncover the distinct transcriptional regulations within the highly suppressive T_{reg} subpopulation. Our unbiased network analyses characterized the high expression of BATF as characteristic of highly activated T_{regs} in the TME and revealed the potential role of *BATF* in modulating T_{reg} migration, activation, and function within the GRN by regulating *CXCR6*, *TNFRSF4*, *TNFRSF9*, *RELB*, *ICOS*, and *CTLA4*, among others. Consistent with results from other T cell subsets, BATF plays a complex role in governing human activated T_{reg} function. We found that BATF promotes activated T_{reg} survival and cellular trafficking while simultaneously limiting excessive activation of T_{regs}. Perturbation of BATF signaling in T_{regs} results in substantial changes of cell surface phenotypes and suppressive function.

Our CRISPR-Cas9 RNP KO approach allowed us to experimentally validate the *BATF*-driven GRN identified in our scRNA-seq analyses and to determine the functional consequences of modulating this network. We leveraged an in vitro system to mimic the persistent antigenic stimulation and metabolic stress T_{regs} experience in the TME. These T_{regs} appeared to mimic features of exhaustion, raising the possibility that this might be a relevant phenotype for intratumoral T_{regs}, highlighting the value for this system to mimic conditions within the TME. The disruption of *BATF* in human primary activated T_{regs}

and T_{regs} with continuous TCR stimulation under hypoxia resulted in distinct phenotypic changes, reflecting the importance of the *BATF*-driven GRN in intratumoral $TNFR^+$ T_{regs}. CRISPR-editing results revealed an enhancement of immunosuppression and activation in *BATF* KO activated T_{regs} accompanied with increased expression of 4–1BB, OX40, ICOS, LAG3, NRP1, and BCL2. We also observed a reduction of CD39 and CD96, indicating that *BATF* functions as a transcriptional nexus in human activated T_{regs} that is essential for T_{reg} activation, function, stability, and survival. Although we went to considerable effort to try to KO *BATF* in human T_{regs} isolated by HNSCC samples using current CRISPR technology, we were unable to recover enough cells with acceptable viability. Future studies should seek to disrupt BATF in activated TIL T_{regs} specifically to interrogate the roles of BATF modulating the activation and function of activated T_{regs} from patients with cancer.

Therapeutic targeting of TIL T_{regs} in cancer without affecting immune homeostasis has been challenging. We show that $TNFR^+$ T_{regs} are frequently found and are associated with worse prognosis across numerous solid tumors. In addition, several surface markers including CD96, CD39, and CD74 were identified on $TNFR^+$ T_{regs} that are preferentially expressed by HNSCC TIL T_{regs}, suggesting a possible path to selectively targeting suppressive TIL T_{regs} without causing overt autoimmunity in normal tissues. A deeper understanding of transcriptional networks that govern T_{reg} function will likely provide opportunities for the treatment of cancer and may identify ways to promote T_{reg} function for the treatment of autoimmunity and inflammatory diseases.

MATERIALS AND METHODS

Study design

The objective of this study was to reconstruct transcriptional networks of suppressive TIL T_{regs} in the TME and identify key regulators that control TIL T_{reg} function and activation. Tumors from patients with HNSCC were acquired under the University of Pittsburgh Cancer Institute Institutional Review Board (IRB)–approved protocol 99-069, with written informed consent obtained from each patient. Nontumor tonsil tissues from patients with sleep apnea or tonsilitis were collected on the same IRB-approved protocol. Tumors from patients with lung cancer were acquired under IRB–approved protocol MODCR19060269-008. HD peripheral blood was collected by venipuncture, using EDTA as the anticoagulant.

Data file S1, tab data S5, summarizes the clinical characteristics of participants, including their sex and age. scRNA-seq was performed to characterize distinct transcriptional signatures and cell states of TIL T_{regs} compared with nontumor tissue T_{regs}, peripheral T_{regs}, and all T_{conv}. CIBERSORTx and TCGA survival analyses were performed to identify subpopulations of TIL T_{regs} that were associated with patient survival outcomes. SCENIC, directed MGM, and FCI-MAX were performed to construct the GRN of $TNFR^+$ T_{regs}. Bioinformatic analyses on two independent scRNA-seq datasets were performed to validate the findings in the HNSCC TME. CRISPR-Cas9 RNP KO was performed to perturb *BATF* signaling in human primary activated T_{regs}. Bulk RNA-seq was performed to globally dissect the transcriptional changes in human activated T_{regs} with *BATF* deletion. In vitro microsuppression assays were performed to interrogate the functional changes of *BATF* KO activated T_{regs}. Flow cytometry staining with TIL and PBMC from patients were performed

to validate and identify additional surface markers that characterize TNFR^{+} T$_{regs}$. Detailed method is included in the Supplementary Materials.

Blood and tissue sample processing

PBMCs were isolated from whole blood by density gradient centrifugation in Ficoll/Hypaque for 20 min at 400*g* with the brake off. Carryover red blood cells were lysed with BD Pharm Lyse, and samples were then resuspended in staining buffer. Single-cell suspensions from tonsil tissues were generated by mechanical disruption followed by enzymatic digestion in serum-free RPMI media. After initial isolation from tissue, cells were passed through a 100-μm filter and spun down to yield single-cell suspensions. Cells were stained and sorted for live CD4^{+} T$_{conv}$ (CD4^{+}CD25^{-} CD127^{high}) and T$_{regs}$ (CD4^{+}CD25^{high}CD127^{low}) by fluorescence-activated cell sorting (FACS) on the Sony MA900 at the Hillman Cancer Center Cytometry Facility. Data file S1, tab data S6, summarizes the detailed information of antibodies used for cell sorting.

scRNA-seq library preparation and sequencing

Immediately after sorting, T$_{conv}$ and T$_{regs}$ were centrifuged for 5 min at 500*g* and were resuspended in phosphate-buffered saline (PBS) with 0.04% bovine serum albumin. Cells were then counted using the Cellometer Auto2000 (Nexcelom) and loaded into the 10X Controller (10X Genomics) targeting a recovery of 2000 cells per sample. The RNA capture, barcoding, cDNA, and library preparation were performed according to the manufacturer's recommendations. The 10x libraries were pooled and sequenced on either a NextSeq500 at the Health Sciences Sequencing Core at Children's Hospital of Pittsburgh or on a NovaSeq6000 at the University of Pittsburgh Medical Center (UPMC) Genome Core. Data file S1 (tab data S1) summarizes the final cell number per participant analyzed in the study after QC.

T$_{reg}$ isolation and expansion

Human umbilical cord samples were collected from the umbilical vein immediately after vaginal delivery by the Obstetric Specimen Procurement Unit at UPMC Magee-Womens Research Institute. PBMC isolation followed the same procedures as described above. T$_{regs}$ from cord blood PBMCs were enriched by a kit and purified again by FACS. Freshly isolated T$_{regs}$ were cultured in complete RPMI. T$_{regs}$ were expanded for 7 days. Data file S1 (tab, Data S6) summarizes the detailed information of antibodies used for cell sorting and T cell activation.

In vitro human T$_{reg}$ culture with TCR stimulation in hypoxia

T$_{regs}$ from cord blood were isolated as shown above. T$_{regs}$ were then activated at 20,000 cells per 96-well round-bottom plates with an equivalent number of Dynabeads in the presence of IL-2 (1000 U/ml) in 200 μl of cRPMI. After 24-hour activation, T$_{regs}$ were expanded with IL-2 only (acute TCR stimulation) or cocultured with 10-fold Dynabeads and IL-2 (continuous TCR stimulation). T$_{regs}$ under acute or continuous TCR activation were cultured in either normoxic (18.6% O_2) or hypoxic (1.5% O_2) gas atmosphere conditions for 10 days.

Cas9 RNP assembly and electroporation

crRNA and trans-activating RNA (tracrRNA) were mixed in a 1:1 ratio and incubated for 30 min at 37°C to generate crRNA–tracrRNA CRISPR duplex. Cas9 protein (Thermo Fisher Scientific) was mixed with the crRNA–tracrRNA duplex and incubated for 15 min at 37°C to generate Cas9 RNP. Expanded human T_{regs} were pelleted and resuspended in P3 buffer. Then, Cas9 RNP and electroporation enhancer (Integrated DNA Technologies) were added directly to the cells and transferred to a 16-well reaction cuvette (Lonza). T_{regs} were electroporated using program EH-115 on the Amaxa 4D-Nucleofector (Lonza). Prewarmed cRPMI was immediately added to each well after electroporation. CRISPR-edited T_{regs} were then rested with cRPMI supplemented with human IL-2 (200 UI/ml) for 48 hours at 37°C. CRISPR-edited T_{regs} and scrambled control T_{regs} were then activated for 72 hours with TCR stimulation. Data file S1, tab data S7, summarizes the sequences of guides used in the experiments.

In vitro microsuppression assay

Naïve $CD8^+$ T cells were isolated by a T cell isolation kit, and antigen-presenting cells (APCs) were isolated by FACS from HD PBMCs. Isolated naïve $CD8^+$ T cells were then labeled with Cell-Trace Violet (CTV; Invitrogen) for 10 min at 37°C. After a 72-hour TCR restimulation, CRISPR-treated T_{regs} were purified again by FACS. Two thousand CRISPR-edited T_{regs} in 50 ml of cRPMI were seeded in the first column of a round-bottom 96-well plate. A serial twofold dilution of T_{regs} was conducted for nine columns. Two thousand APCs and 2000 CTV-labeled naïve $CD8^+$ T cells in 50 ml of cRPMI were added separately to all wells to change the T_{regs}:$CD8^+$ T cell ratio from 1:2 to 1:1000. Fifty milliliters of cRPMI supplemented with anti-CD3 (2 μg/ml) were then added to all wells. Cells were cultured for 5 days at 37°C with 5% CO_2. Then, cells were spun down and stained for flow cytometry analysis.

Surface and intracellular antibody staining

CRISPR-edited T_{regs}, scrambled controls, and unperturbed controls were resuspended in staining buffer and labeled with antibodies at 1:100 for 25 min at 4°C, followed by viability staining using fixable dye (eFluor 780 viability dye at 1:4000 or Zombie NIR at 1:2000 ratio). Cells were then spun down at 500*g* for 5 min and washed with PBS. Foxp3/Transcription Factor Staining Buffer (eBioscience) was added into cells for 60 min at room temperature for cell fixation. Cells were then washed by permeabilization buffer (eBioscience) and labeled with antibodies for 60 min at room temperature for intracellular staining. Cells were washed with permeabilization buffer and FACS buffer. The BD LSRFortessa II flow cytometer or Cytek Aurora was used for acquiring flow cytometry readouts, and FlowJo V10 was used for data analysis. Data file S1, tab data S6, summarizes the detailed information of antibodies used for flow cytometry.

Bulk RNA-seq

CRISPR-edited T_{regs} and scrambled controls were double-sorted (purity, >99.5%) directly into individual wells of a 96-well plate containing 2 μl of lysis buffer. The plate was spun down at 2000*g* for 2 min, and reverse transcription was then performed. An addition

of 15-cycle complementary DNA amplification was performed after cDNA synthesis by the KAPA Hot Start II High-Fidelity DNA Polymerase. cDNA size was verified with TapeStation D5000 and quantified by the Qubit (Thermo Fisher Scientific). Sequencing libraries were prepared from 1 ng of cDNA using the Nextera XT DNA Library Prep kit (Illumina FC-131-1096), following the manufacturer's instructions. cDNA libraries were quantified by the KAPA library quantification kit (KAPA KK4854), and size was verified on a TapeStation D1000. Ten diluted libraries were pooled and sequenced with the NextSeq 500/550 High Output v.2 kit.

Bulk RNA-seq data analysis

We used the R package DESeq2 (1.40.1) for downstream bulk RNA-seq analysis (66). The batch effects between donors were corrected by ComBat-seq (v3.36.0) (67). Genes were filtered as not expressed if their read count was less than 10. Differential gene analysis was done by DESeq function in DESeq2 (1.40.1). Log_2 fold changes were added into the analysis by lfcShrink function in DESeq2 (1.40.1). Gene set enrichment analysis was performed by using R package clusterProfiler (4.8.1) (68).

scRNA-seq data integration and clustering

We used the R package Seurat v4 for downstream scRNA-seq analysis. The dataset was split by patient and normalized using SCTransform v1 (23). The most variable genes in each patient were identified, and the top 2000 variable genes overlapped across groups were selected for integration. Then, we scaled the integrated dataset to remove confounding sources of variation by regressing out the percentage of mitochondrial genes expressed per cell and the number of genes per cell. Further, we used principal components analysis (PCA) to dimensionally reduce the dataset to 30 dimensions and chose 1 to 20 PCs that explained the most variance in the dataset for visualization and cell clustering. We next performed Louvain graph–based clustering and applied a nonlinear dimensional reduction method UMAP to visualize the dataset. T_{conv} and T_{regs} were identified on the basis of the original paper and previous sorting results.

DE analysis and gene set enrichment analysis

We next used FindAllMarkers function in Seurat to run DE analysis between different groups of T cell subpopulations depending on the comparison. The top DE genes in each subpopulation were ranked on the basis of the log_2 fold change. We then performed the gene set enrichment analysis to T_{regs} in the dataset by using the R package singleseqgset as previously described (19). The log_2 fold change in gene expression was calculated for all genes across T_{reg} clusters and used as input for a variance inflation–corrected Wilcoxon rank sum test to calculate whether the gene sets were up-regulated in a concerted manner within a cluster.

GRN reconstruction

To reconstruct the GRNs within T_{reg} subpopulations, we used SCENIC to infer regulons with normalized data matrices as input. The regulons were generated, and the regulon activities were calculated following the pySCENIC (0.11.2) pipeline (46). We identified

the differentially activated regulons in each T_{reg} subpopulation by the Wilcoxon rank sum test against all the other cells. To identify GRNs central to $TNFR^{+}$ T_{reg} subpopulation, we combined the target genes and regulators in the top five regulons ranked by $\log_2$ fold change and used normalized data metrices as input for the causal MGM (42). We used MGM to build a skeleton network and then FCI-MAX to refine the network and determine correlation (69). Signaling pathways were analyzed by Reactome (70).

Pseudotime analysis

To infer T_{reg} developmental trajectory, we applied the RNAvelocity algorithm to infer pseudotime for each T_{reg} (26, 71). The differentiation trajectory and pseudotime inference were performed by scanpy (version 1.6.1) and scVelo (v0.2.4) (26). To infer the developmental trajectory of T_{regs} from the online published datasets, we applied the Slingshot (72) algorithm to infer pseudotime for each T_{reg}. Briefly, we took the first three PCs from the PCA generated during cell clustering procedure (as described above) and normalized the dataset for input into the R package Slingshot. We used the predefined clustering results to identify the global lineage structure by a cluster-based minimal spanning tree, fitted principal curves to describe each lineage, and lastly aligned cells on a pseudotime trajectory.

Survival analysis using TCGA

To determine whether the enrichment of T_{reg} subpopulations was associated with survival outcomes of patients with cancer, we used bulk RNA-seq data of patients with HNSCC, NSCLC, and melanoma available through TCGA. Similarly, bulk RNA-seq data of normal lung and normal skin (sun exposed) were obtained from GTEx. The enrichment score for each T_{reg} subpopulation from each patient was calculated as previously described (73, 74). The gene set was defined by using the top 200 genes that were differentially expressed in each T_{reg} subpopulation. Enrichment scores were calculated and used as a reference profile to deconvolute bulk RNA-seq data from TCGA and GTEx by CIBERSORTx (30). We then performed monovariate and multivariable analyses based on patients' PFS.

Statistical analysis

Specific statistical analyses including Wilcoxon rank sum test for DE gene analysis, Cox proportional hazard regression for monovariate and multivariable analyses, and Pearson's correlation for gene coexpression and T_{reg} signature analysis were performed using R-4.3.1. Statistical analyses, including two-way analysis of variance (ANOVA) test, nonparametric Mann-Whitney U test, and ratio paired t test for flow cytometry analyses, were performed using GraphPad/Prism v9.

Supplementary Material

Refer to Web version on PubMed Central for supplementary material.

Acknowledgments:

We thank members of the Vignali, Bruno, and Benos Labs for constructive comments and feedback. We thank the Delgoffe Lab for support of the in vitro T cell culture with TCR stimulation in hypoxia. We thank C. Sander and

E. Rush and the Kirkwood lab for assistance in providing clinical samples from patients with melanoma. We thank J. Ward for assistance in providing clinical samples from patients with lung cancer. We thank D. Liu for assistance in coordination and collection of lung cancer specimens. We thank the Hillman Cytometry Facility for assistance with flow cytometry and the Immunology Flow Core for cell sorting. We thank Obstetric Specimen Procurement Unit at UPMC Magee-Womens Research Institute for cord blood samples. This research was supported in part by the University of Pittsburgh Center for Research Computing through the resources provided. Graphical abstract and experimental schematics were designed using Biorender.com.

Funding:

This work was supported by the National Institutes of Health {R35 CA263850, P50 CA254865, and P50 CA097190 [D.A.A.V.], R01 HL159805 and R01 HL157879 [P.V.B.], the Cancer Immunology Training Program T32 [T32 CA082084 (D.A.A.V.), awarded to A.R.C. and D.Y.], and Hillman Postdoctoral Fellowship for Innovative Cancer Research [A.R.C.]}.

Data and materials availability:

All data needed to evaluate the conclusions in the paper are present in the paper or the Supplementary Materials. Codes for all custom algorithms are publicly available in GitHub repositories at: https://github.com/shf43/BATF_Treg_Network. The sequencing datasets generated in this study are deposited at the Gene Expression Omnibus: GSE239750. The previously published datasets discussed in this publication are GSE139324, E-MTAB-8107, E-MTAB-6149, and E-MTAB-6653.

REFERENCES AND NOTES

1. Vignali DA, Collison LW, Workman CJ, How regulatory T cells work. Nat. Rev. Immunol. 8, 523–532 (2008). [PubMed: 18566595]
2. Bennett CL, Christie J, Ramsdell F, Brunkow ME, Ferguson PJ, Whitesell L, Kelly TE, Saulsbury FT, Chance PF, Ochs HD, The immune dysregulation, polyendocrinopathy, enteropathy, X-linked syndrome (IPEX) is caused by mutations of FOXP3. Nat. Genet. 27, 20–21 (2001). [PubMed: 11137993]
3. Liu C, Workman CJ, Vignali DAA, Targeting regulatory T cells in tumors. FEBS J. 283, 2731–2748 (2016). [PubMed: 26787424]
4. Scott EN, Gocher AM, Workman CJ, Vignali DAA, Regulatory T cells: Barriers of immune infiltration into the tumor microenvironment. Front. Immunol. 12, 702726 (2021). [PubMed: 34177968]
5. Liu S, Foulkes WD, Leung S, Gao D, Lau S, Kos Z, Nielsen TO, Prognostic significance of $FOXP3^+$ tumor-infiltrating lymphocytes in breast cancer depends on estrogen receptor and human epidermal growth factor receptor-2 expression status and concurrent cytotoxic T-cell infiltration. Breast Cancer Res. 16, 432 (2014). [PubMed: 25193543]
6. Shang B, Liu Y, Jiang S-J, Liu Y, Prognostic value of tumor-infiltrating $FoxP3^+$ regulatory T cells in cancers: A systematic review and meta-analysis. Sci. Rep. 5, 15179 (2015). [PubMed: 26462617]
7. Curiel TJ, Coukos G, Zou L, Alvarez X, Cheng P, Mottram P, Evdemon-Hogan M, Conejo-Garcia JR, Zhang L, Burow M, Zhu Y, Wei S, Kryczek I, Daniel B, Gordon A, Myers L, Lackner A, Disis ML, Knutson KL, Chen L, Zou W, Specific recruitment of regulatory T cells in ovarian carcinoma fosters immune privilege and predicts reduced survival. Nat. Med. 10, 942–949 (2004). [PubMed: 15322536]
8. Leffers N, Gooden MJM, de Jong RA, Hoogeboom BN, ten Hoor KA, Hollema H, Boezen HM, van der Zee AGJ, Daemen T, Nijman HW, Prognostic significance of tumor-infiltrating T-lymphocytes in primary and metastatic lesions of advanced stage ovarian cancer. Cancer Immunol. Immunother. 58, 449–459 (2009). [PubMed: 18791714]
9. West NR, Kost SE, Martin SD, Milne K, deLeeuw RJ, Nelson BH, Watson PH, Tumour-infiltrating $FOXP3^+$ lymphocytes are associated with cytotoxic immune responses and good clinical outcome in oestrogen receptor-negative breast cancer. Br. J. Cancer 108, 155–162 (2013). [PubMed: 23169287]

10. Shan F, Somasundaram A, Bruno TC, Workman CJ, Vignali DAA, Therapeutic targeting of regulatory T cells in cancer. Trends Cancer 8, 944–961 (2022). [PubMed: 35853825]
11. Rech AJ, Mick R, Martin S, Recio A, Aqui NA, Powell DJ Jr., Colligon TA, Trosko JA, Leinbach LI, Pletcher CH, Tweed CK, DeMichele A, Fox KR, Domchek SM, Riley JL, Vonderheide RH, CD25 blockade depletes and selectively reprograms regulatory T cells in concert with immunotherapy in cancer patients. Sci. Transl. Med. 4, 134ra162 (2012).
12. Zappasodi R, Sirard C, Li Y, Budhu S, Abu-Akeel M, Liu C, Yang X, Zhong H, Newman W, Qi J, Wong P, Schaer D, Koon H, Velcheti V, Hellmann MD, Postow MA, Callahan MK, Wolchok JD, Merghoub T, Rational design of anti-GITR-based combination immunotherapy. Nat. Med. 25, 759–766 (2019). [PubMed: 31036879]
13. Hirschhorn-Cymerman D, Rizzuto GA, Merghoub T, Cohen AD, Avogadri F, Lesokhin AM, Weinberg AD, Wolchok JD, Houghton AN, OX40 engagement and chemotherapy combination provides potent antitumor immunity with concomitant regulatory T cell apoptosis. J. Exp. Med. 206, 1103–1116 (2009). [PubMed: 19414558]
14. Dépis F, Hu C, Weaver J, McGrath L, Klebanov B, Buggé J, Umiker B, Fregeau C, Upadhyay D, Singh A, Xu CA, Spaulding V, Priess M, Wong M, Naheed S, Zhang Y, Legendre K, Stack EC, Mora A, Willer M, Meetze K, Gostissa M, Meehl MA, Shaffer DR, Abstract 4532: Preclinical evaluation of JTX-1811, an anti-CCR8 antibody with enhanced ADCC activity, for preferential depletion of tumor-infiltrating regulatory T cells. Cancer Res. 80, 4532–4532 (2020).
15. Friedman C, Ascierto P, Davar D, O'Hara M, Shapira-Frommer R, Dallos M, Khemka V, James L, Fischer B, Demes S, Li L, Kozicki M, Ravindran P, Xu K, Kollia G, Shoukry J, Yunan M, Massey A, Gutierrez M, 393 First-in-human phase 1/2a study of the novel nonfucosylated anti–CTLA-4 monoclonal antibody BMS-986218 ± nivolumab in advanced solid tumors: Initial phase 1 results. J. Immunother. Cancer 8, A239 (2020).
16. Infante JR, Hansen AR, Pishvaian MJ, Chow LQM, McArthur GA, Bauer TM, Liu SV, Sandhu SK, Tsai FYC, Kim J, Stefanich E, Li CC, Gilbert H, MCCALL B, Anderson MS, Huseni M, Rhee IP, Siu LL, Gordon MS, A phase Ib dose escalation study of the OX40 agonist MOXR0916 and the PD-L1 inhibitor atezolizumab in patients with advanced solid tumors. J. Clin. Oncol. 34, 101–101 (2016).
17. Diab A, Hamid O, Thompson JA, Ros W, Eskens FALM, Doi T, Hu-Lieskovan S, Klempner SJ, Ganguly B, Fleener C, Wang X, Joh T, Liao K, Salek-Ardakani S, Taylor CT, Chou J, el-Khoueiry AB, A Phase I, Open-Label, Dose-Escalation Study of the OX40 Agonist Ivuxolimab in Patients with Locally Advanced or Metastatic Cancers. Clin. Cancer Res. 28, 71–83 (2022). [PubMed: 34615725]
18. Jacobs JFM, Punt CJA, Lesterhuis WJ, Sutmuller RPM, Brouwer HM-LH, Scharenborg NM, Klasen IS, Hilbrands LB, Figdor CG, de Vries IJM, Adema GJ, Dendritic cell vaccination in combination with anti-CD25 monoclonal antibody treatment: A phase I/II study in metastatic melanoma patients. Clin. Cancer Res. 16, 5067–5078 (2010). [PubMed: 20736326]
19. Cillo AR, Kürten CHL, Tabib T, Qi Z, Onkar S, Wang T, Liu A, Duvvuri U, Kim S, Soose RJ, Oesterreich S, Chen W, Lafyatis R, Bruno TC, Ferris RL, Vignali DAA, Immune Landscape of Viral- and Carcinogen-Driven Head and Neck Cancer. Immunity 52, 183–199.e9 (2020). [PubMed: 31924475]
20. Saito T, Nishikawa H, Wada H, Nagano Y, Sugiyama D, Atarashi K, Maeda Y, Hamaguchi M, Ohkura N, Sato E, Nagase H, Nishimura J, Yamamoto H, Takiguchi S, Tanoue T, Suda W, Morita H, Hattori M, Honda K, Mori M, Doki Y, Sakaguchi S, Two $FOXP3^+CD4^+$ T cell subpopulations distinctly control the prognosis of colorectal cancers. Nat. Med. 22, 679–684 (2016). [PubMed: 27111280]
21. Miyara M, Yoshioka Y, Kitoh A, Shima T, Wing K, Niwa A, Parizot C, Taflin C, Heike T, Valeyre D, Mathian A, Nakahata T, Yamaguchi T, Nomura T, Ono M, Amoura Z, Gorochov G, Sakaguchi S, Functional delineation and differentiation dynamics of human $CD4^+$ T cells expressing the FoxP3 transcription factor. Immunity 30, 899–911 (2009). [PubMed: 19464196]
22. Chen X, Subleski JJ, Kopf H, Howard OMZ, Männel DN, Oppenheim JJ, Cutting edge: Expression of TNFR2 defines a maximally suppressive subset of mouse $CD4^+CD25^+FoxP3^+$ T regulatory cells: Applicability to tumor-infiltrating T regulatory cells. J. Immunol. 180, 6467–6471 (2008). [PubMed: 18453563]

23. Hao Y, Hao S, Andersen-Nissen E, Mauck III WM, Zheng S, Butler A, Lee MJ, Wilk AJ, Darby C, Zager M, Hoffman P, Stoeckius M, Papalexi E, Mimitou EP, Jain J, Srivastava A, Stuart T, Fleming LM, Yeung B, Rogers AJ, McElrath JM, Blish CA, Gottardo R, Smibert P, Satija R, Integrated analysis of multimodal single-cell data. Cell 184, 3573–3587.e29 (2021). [PubMed: 34062119]
24. Vasanthakumar A, Liao Y, Teh P, Pascutti MF, Oja AE, Garnham AL, Gloury R, Tempany JC, Sidwell T, Cuadrado E, Tuijnenburg P, Kuijpers TW, Lalaoui N, Mielke LA, Bryant VL, Hodgkin PD, Silke J, Smyth GK, Nolte MA, Shi W, Kallies A, The TNF receptor superfamily-NF-κB axis is critical to maintain effector regulatory t cells in lymphoid and non-lymphoid tissues. Cell Rep. 20, 2906–2920 (2017). [PubMed: 28889989]
25. Lambert SA, Jolma A, Campitelli LF, das PK, Yin Y, Albu M, Chen X, Taipale J, Hughes TR, Weirauch MT, The Human Transcription Factors. Cell 172, 650–665 (2018). [PubMed: 29425488]
26. Bergen V, Lange M, Peidli S, Wolf FA, Theis FJ, Generalizing RNA velocity to transient cell states through dynamical modeling. Nat. Biotechnol. 38, 1408–1414 (2020). [PubMed: 32747759]
27. Sjaastad LE, Owen DL, LaRue RS, Farrar MA, Interferons in Treg development and function. J. Immunol. 204, 228.17 (2020).
28. Levine AG, Mendoza A, Hemmers S, Moltedo B, Niec RE, Schizas M, Hoyos BE, Putintseva EV, Chaudhry A, Dikiy S, Fujisawa S, Chudakov DM, Treuting PM, Rudensky AY, Stability and function of regulatory T cells expressing the transcription factor T-bet. Nature 546, 421–425 (2017). [PubMed: 28607488]
29. Gocher-Demske AM, Cui J, Szymczak-Workman AL, Vignali KM, Latini JN, Pieklo GP, Kimball JC, Avery L, Cipolla EM, Huckestein BR, Hedden L, Meisel M, Alcorn JF, Kane LP, Workman CJ, Vignali DAA, IFNγ-induction of TH1-like regulatory T cells controls antiviral responses. Nat. Immunol. 24, 841–854 (2023). [PubMed: 36928412]
30. Newman AM, Steen CB, Liu CL, Gentles AJ, Chaudhuri AA, Scherer F, Khodadoust MS, Esfahani MS, Luca BA, Steiner D, Diehn M, Alizadeh AA, Determining cell type abundance and expression from bulk tissues with digital cytometry. Nat. Biotechnol. 37, 773–782 (2019). [PubMed: 31061481]
31. Aibar S, González-Blas CB, Moerman T, Huynh-Thu VA, Imrichova H, Hulselmans G, Rambow F, Marine JC, Geurts P, Aerts J, van den Oord J, Atak ZK, Wouters J, Aerts S, SCENIC: Single-cell regulatory network inference and clustering. Nat. Methods 14, 1083–1086 (2017). [PubMed: 28991892]
32. Konopacki C, Pritykin Y, Rubtsov Y, Leslie CS, Rudensky AY, Transcription factor Foxp1 regulates Foxp3 chromatin binding and coordinates regulatory T cell function. Nat. Immunol. 20, 232–242 (2019). [PubMed: 30643266]
33. Sebzda E, Zou Z, Lee JS, Wang T, Kahn ML, Transcription factor KLF2 regulates the migration of naive T cells by restricting chemokine receptor expression patterns. Nat. Immunol. 9, 292–300 (2008). [PubMed: 18246069]
34. Zemmour D, Zilionis R, Kiner E, Klein AM, Mathis D, Benoist C, Single-cell gene expression reveals a landscape of regulatory T cell phenotypes shaped by the TCR. Nat. Immunol. 19, 291–301 (2018). [PubMed: 29434354]
35. Wang Z, Zheng Y, Hou C, Yang L, Li X, Lin J, Huang G, Lu Q, Wang CY, Zhou Z, DNA methylation impairs TLR9 induced Foxp3 expression by attenuating IRF-7 binding activity in fulminant type 1 diabetes. J. Autoimmun. 41, 50–59 (2013). [PubMed: 23490285]
36. Roessner PM, Llaó Cid L, Lupar E, Roider T, Bordas M, Schifflers C, Arseni L, Gaupel AC, Kilpert F, Krötschel M, Arnold SJ, Sellner L, Colomer D, Stilgenbauer S, Dietrich S, Lichter P, Izcue A, Seiffert M, EOMES and IL-10 regulate antitumor activity of T regulatory type 1 CD4+ T cells in chronic lymphocytic leukemia. Leukemia 35, 2311–2324 (2021). [PubMed: 33526861]
37. Ruan Q, Chen YH, Nuclear factor-κB in immunity and inflammation: The Treg and Th17 connection. Adv. Exp. Med. Biol. 946, 207–221 (2012). [PubMed: 21948370]
38. Ronin E, Lubrano di Ricco M, Vallion R, Divoux J, Kwon HK, Grégoire S, Collares D, Rouers A, Baud V, Benoist C, Salomon BL, The NF-κB RelA Transcription Factor Is Critical for Regulatory T Cell Activation and Stability. Front. Immunol. 10, 2487 (2019). [PubMed: 31749798]

39. Grinberg-Bleyer Y, Caron R, Seeley JJ, de Silva NS, Schindler CW, Hayden MS, Klein U, Ghosh S, The Alternative NF-κB Pathway in Regulatory T Cell Homeostasis and Suppressive Function. J. Immunol. 200, 2362–2371 (2018). [PubMed: 29459403]
40. Singh Y, Garden OA, Lang F, Cobb BS, MicroRNAs regulate T-cell production of interleukin-9 and identify hypoxia-inducible factor-2α as an important regulator of T helper 9 and regulatory T-cell differentiation. Immunology 149, 74–86 (2016). [PubMed: 27278750]
41. Hsu T-S, Lin YL, Wang YA, Mo ST, Chi PY, Lai ACY, Pan HY, Chang YJ, Lai MZ, HIF-2α is indispensable for regulatory T cell function. Nat. Commun. 11, 5005 (2020). [PubMed: 33024109]
42. Sedgewick AJ, Buschur K, Shi I, Ramsey JD, Raghu VK, Manatakis DV, Zhang Y, Bon J, Chandra D, Karoleski C, Sciurba FC, Spirtes P, Glymour C, Benos PV, Mixed graphical models for integrative causal analysis with application to chronic lung disease diagnosis and prognosis. Bioinformatics 35, 1204–1212 (2019). [PubMed: 30192904]
43. Plaza-Sirvent C, Schuster M, Neumann Y, Heise U, Pils MC, Schulze-Osthoff K, Schmitz I, c-FLIP Expression in Foxp3-Expressing Cells Is Essential for Survival of Regulatory T Cells and Prevention of Autoimmunity. Cell Rep. 18, 12–22 (2017). [PubMed: 28052242]
44. Beharry Z, Mahajan S, Zemskova M, Lin YW, Tholanikunnel BG, Xia Z, Smith CD, Kraft AS, The Pim protein kinases regulate energy metabolism and cell growth. Proc. Natl. Acad. Sci. U.S.A. 108, 528–533 (2011). [PubMed: 21187426]
45. Miragaia RJ, Gomes T, Chomka A, Jardine L, Riedel A, Hegazy AN, Whibley N, Tucci A, Chen X, Lindeman I, Emerton G, Krausgruber T, Shields J, Haniffa M, Powrie F, Teichmann SA, Single-Cell Transcriptomics of Regulatory T Cells Reveals Trajectories of Tissue Adaptation. Immunity 50, 493–504.e7 (2019). [PubMed: 30737144]
46. Van de Sande B, Flerin C, Davie K, De Waegeneer M, Hulselmans G, Aibar S, Seurinck R, Saelens W, Cannoodt R, Rouchon Q, Verbeiren T, De Maeyer D, Reumers J, Saeys Y, Aerts S, A scalable SCENIC workflow for single-cell gene regulatory network analysis. Nat. Protoc. 15, 2247–2276 (2020). [PubMed: 32561888]
47. Qian J, Olbrecht S, Boeckx B, Vos H, Laoui D, Etlioglu E, Wauters E, Pomella V, Verbandt S, Busschaert P, Bassez A, Franken A, Bempt MV, Xiong J, Weynand B, van Herck Y, Antoranz A, Bosisio FM, Thienpont B, Floris G, Vergote I, Smeets A, Tejpar S, Lambrechts D, A pan-cancer blueprint of the heterogeneous tumor microenvironment revealed by single-cell profiling. Cell Res. 30, 745–762 (2020). [PubMed: 32561858]
48. Schumann K, Raju SS, Lauber M, Kolb S, Shifrut E, Cortez JT, Skartsis N, Nguyen VQ, Woo JM, Roth TL, Yu R, Nguyen MLT, Simeonov DR, Nguyen DN, Targ S, Gate RE, Tang Q, Bluestone JA, Spitzer MH, Ye CJ, Marson A, Functional CRISPR dissection of gene networks controlling human regulatory T cell identity. Nat. Immunol. 21, 1456–1466 (2020). [PubMed: 32989329]
49. Chen Z, Chen Y, Zhou J, Li Y, Gong C, Wang X, Netrin-1 reduces lung ischemia-reperfusion injury by increasing the proportion of regulatory T cells. J. Int. Med. Res. 48, 300060520926415 (2020). [PubMed: 32485133]
50. Delgoffe GM, Woo SR, Turnis ME, Gravano DM, Guy C, Overacre AE, Bettini ML, Vogel P, Finkelstein D, Bonnevier J, Workman CJ, Vignali DAA, Stability and function of regulatory T cells is maintained by a neuropilin-1-semaphorin-4a axis. Nature 501, 252–256 (2013). [PubMed: 23913274]
51. Scharping NE, Rivadeneira DB, Menk AV, Vignali PDA, Ford BR, Rittenhouse NL, Peralta R, Wang Y, Wang Y, DePeaux K, Poholek AC, Delgoffe GM, Mitochondrial stress induced by continuous stimulation under hypoxia rapidly drives T cell exhaustion. Nat. Immunol. 22, 205–215 (2021). [PubMed: 33398183]
52. Zheng L, Qin S, Si W, Wang A, Xing B, Gao R, Ren X, Wang L, Wu X, Zhang J, Wu N, Zhang N, Zheng H, Ouyang H, Chen K, Bu Z, Hu X, Ji J, Zhang Z, Pan-cancer single-cell landscape of tumor-infiltrating T cells. Science 374, abe6474 (2021). [PubMed: 34914499]
53. Lam JH, Hong M, Koo SL, Chua CWL, Lim KL, Wee F, Wan WK, Leow WQ, Yeo JG, Tan IBH, Yeong J, Lim TKH, Lim TS, $CD30^{+}OX40^{+}$ Treg is associated with improved overall survival in colorectal cancer. Cancer Immunol. Immunother. 70, 2353–2365 (2021). [PubMed: 33527196]
54. Sukumar S, Wilson DC, Yu Y, Wong J, Naravula S, Ermakov G, Riener R, Bhagwat B, Necheva AS, Grein J, Churakova T, Mangadu R, Georgiev P, Manfra D, Pinheiro EM, Sriram V, Bailey WJ, Herzyk D, McClanahan TK, Willingham A, Beebe AM, Sadekova S, Characterization of

MK-4166, a Clinical Agonistic Antibody That Targets Human GITR and Inhibits the Generation and Suppressive Effects of T Regulatory Cells. Cancer Res. 77, 4378–4388 (2017). [PubMed: 28611044]

55. Tanaka A, Sakaguchi S, Targeting Treg cells in cancer immunotherapy. Eur. J. Immunol. 49, 1140–1146 (2019). [PubMed: 31257581]
56. Boothby IC, Cohen JN, Rosenblum MD, Regulatory T cells in skin injury: At the crossroads of tolerance and tissue repair. Sci. Immunol. 5, eaaz9631 (2020). [PubMed: 32358172]
57. Traxinger BR, Richert-Spuhler LE, Lund JM, Mucosal tissue regulatory T cells are integral in balancing immunity and tolerance at portals of antigen entry. Mucosal Immunol. 15, 398–407 (2022). [PubMed: 34845322]
58. Itahashi K, Irie T, Yuda J, Kumagai S, Tanegashima T, Lin YT, Watanabe S, Goto Y, Suzuki J, Aokage K, Tsuboi M, Minami Y, Ishii G, Ohe Y, Ise W, Kurosaki T, Suzuki Y, Koyama S, Nishikawa H, BATF epigenetically and transcriptionally controls the activation program of regulatory T cells in human tumors. Sci. Immunol. 7, eabk0957 (2022). [PubMed: 36206353]
59. Yan M, Hu J, Yuan H, Xu L, Liao G, Jiang Z, Zhu J, Pang B, Ping Y, Zhang Y, Xiao Y, Li X, Dynamic regulatory networks of T cell trajectory dissect transcriptional control of T cell state transition. Mol. Ther. Nucleic Acids 26, 1115–1129 (2021). [PubMed: 34786214]
60. Kurachi M, Barnitz RA, Yosef N, Odorizzi PM, DiIorio MA, Lemieux ME, Yates K, Godec J, Klatt MG, Regev A, Wherry EJ, Haining WN, The transcription factor BATF operates as an essential differentiation checkpoint in early effector $CD8^+$ T cells. Nat. Immunol. 15, 373–383 (2014). [PubMed: 24584090]
61. Ise W, Kohyama M, Schraml BU, Zhang T, Schwer B, Basu U, Alt FW, Tang J, Oltz EM, Murphy TL, Murphy KM, The transcription factor BATF controls the global regulators of class-switch recombination in both B cells and T cells. Nat. Immunol. 12, 536–543 (2011). [PubMed: 21572431]
62. Schraml BU, Hildner K, Ise W, Lee WL, Smith WAE, Solomon B, Sahota G, Sim J, Mukasa R, Cemerski S, Hatton RD, Stormo GD, Weaver CT, Russell JH, Murphy TL, Murphy KM, The AP-1 transcription factor Batf controls TH17 differentiation. Nature 460, 405–409 (2009). [PubMed: 19578362]
63. Quigley M, Pereyra F, Nilsson B, Porichis F, Fonseca C, Eichbaum Q, Julg B, Jesneck JL, Brosnahan K, Imam S, Russell K, Toth I, Piechocka-Trocha A, Dolfi D, Angelosanto J, Crawford A, Shin H, Kwon DS, Zupkosky J, Francisco L, Freeman GJ, Wherry EJ, Kaufmann DE, Walker BD, Ebert B, Haining WN, Transcriptional analysis of HIV-specific $CD8^+$ T cells shows that PD-1 inhibits T cell function by upregulating BATF. Nat. Med. 16, 1147–1151 (2010). [PubMed: 20890291]
64. Hayatsu N, Miyao T, Tachibana M, Murakami R, Kimura A, Kato T, Kawakami E, Endo TA, Setoguchi R, Watarai H, Nishikawa T, Yasuda T, Yoshida H, Hori S, Analyses of a Mutant Foxp3 Allele Reveal BATF as a Critical Transcription Factor in the Differentiation and Accumulation of Tissue Regulatory T Cells. Immunity 47, 268–283.e9 (2017). [PubMed: 28778586]
65. Vasanthakumar A, Moro K, Xin A, Liao Y, Gloury R, Kawamoto S, Fagarasan S, Mielke LA, Afshar-Sterle S, Masters SL, Nakae S, Saito H, Wentworth JM, Li P, Liao W, Leonard WJ, Smyth GK, Shi W, Nutt SL, Koyasu S, Kallies A, The transcriptional regulators IRF4, BATF and IL-33 orchestrate development and maintenance of adipose tissue-resident regulatory T cells. Nat. Immunol. 16, 276–285 (2015). [PubMed: 25599561]
66. Love MI, Huber W, Anders S, Moderated estimation of fold change and dispersion for RNA-seq data with DESeq2. Genome Biol. 15, 550 (2014). [PubMed: 25516281]
67. Zhang Y, Parmigiani G, Johnson WE, ComBat-seq: Batch effect adjustment for RNA-seq count data. NAR Genom. Bioinform. 2, lqaa078 (2020). [PubMed: 33015620]
68. Wu T, Hu E, Xu S, Chen M, Guo P, Dai Z, Feng T, Zhou L, Tang W, Zhan L, Fu X, Liu S, Bo X, Yu G, clusterProfiler 4.0: A universal enrichment tool for interpreting omics data. Innovation (Camb) 2, 100141 (2021). [PubMed: 34557778]
69. Raghu VK, Ramsey JD, Morris A, Manatakis DV, Sprites P, Chrysanthis PK, Glymour C, Benos PV, Comparison of strategies for scalable causal discovery of latent variable models from mixed data. Int. J. Data Sci. Anal. 6, 33–45 (2018). [PubMed: 30148202]

70. Gillespie M, Jassal B, Stephan R, Milacic M, Rothfels K, Senff-Ribeiro A, Griss J, Sevilla C, Matthews L, Gong C, Deng C, Varusai T, Ragueneau E, Haider Y, May B, Shamovsky V, Weiser J, Brunson T, Sanati N, Beckman L, Shao X, Fabregat A, Sidiropoulos K, Murillo J, Viteri G, Cook J, Shorser S, Bader G, Demir E, Sander C, Haw R, Wu G, Stein L, Hermjakob H, D'Eustachio P, The reactome pathway knowledgebase 2022. Nucleic Acids Res. 50, D687–D692 (2022). [PubMed: 34788843]

71. La Manno G, Soldatov R, Zeisel A, Braun E, Hochgerner H, Petukhov V, Lidschreiber K, Kastriti ME, Lönnerberg P, Furlan A, Fan J, Borm LE, Liu Z, van Bruggen D, Guo J, He X, Barker R, Sundström E, Castelo-Branco G, Cramer P, Adameyko I, Linnarsson S, Kharchenko PV, RNA velocity of single cells. Nature 560, 494–498 (2018). [PubMed: 30089906]

72. Street K, Risso D, Fletcher RB, das D, Ngai J, Yosef N, Purdom E, Dudoit S, Slingshot: Cell lineage and pseudotime inference for single-cell transcriptomics. BMC Genomics 19, 477 (2018). [PubMed: 29914354]

73. Zhang Q, Chikina M, Szymczak-Workman AL, Horne W, Kolls JK, Vignali KM, Normolle D, Bettini M, Workman CJ, Vignali DAA, LAG3 limits regulatory T cell proliferation and function in autoimmune diabetes. Sci. Immunol. 2, eaah4569 (2017). [PubMed: 28783703]

74. Ruffin AT, Cillo AR, Tabib T, Liu A, Onkar S, Kunning SR, Lampenfeld C, Atiya HI, Abecassis I, Kürten CHL, Qi Z, Soose R, Duvvuri U, Kim S, Oesterrich S, Lafyatis R, Coffman LG, Ferris RL, Vignali DAA, Bruno TC, B cell signatures and tertiary lymphoid structures contribute to outcome in head and neck squamous cell carcinoma. Nat. Commun. 12, 3349 (2021). [PubMed: 34099645]

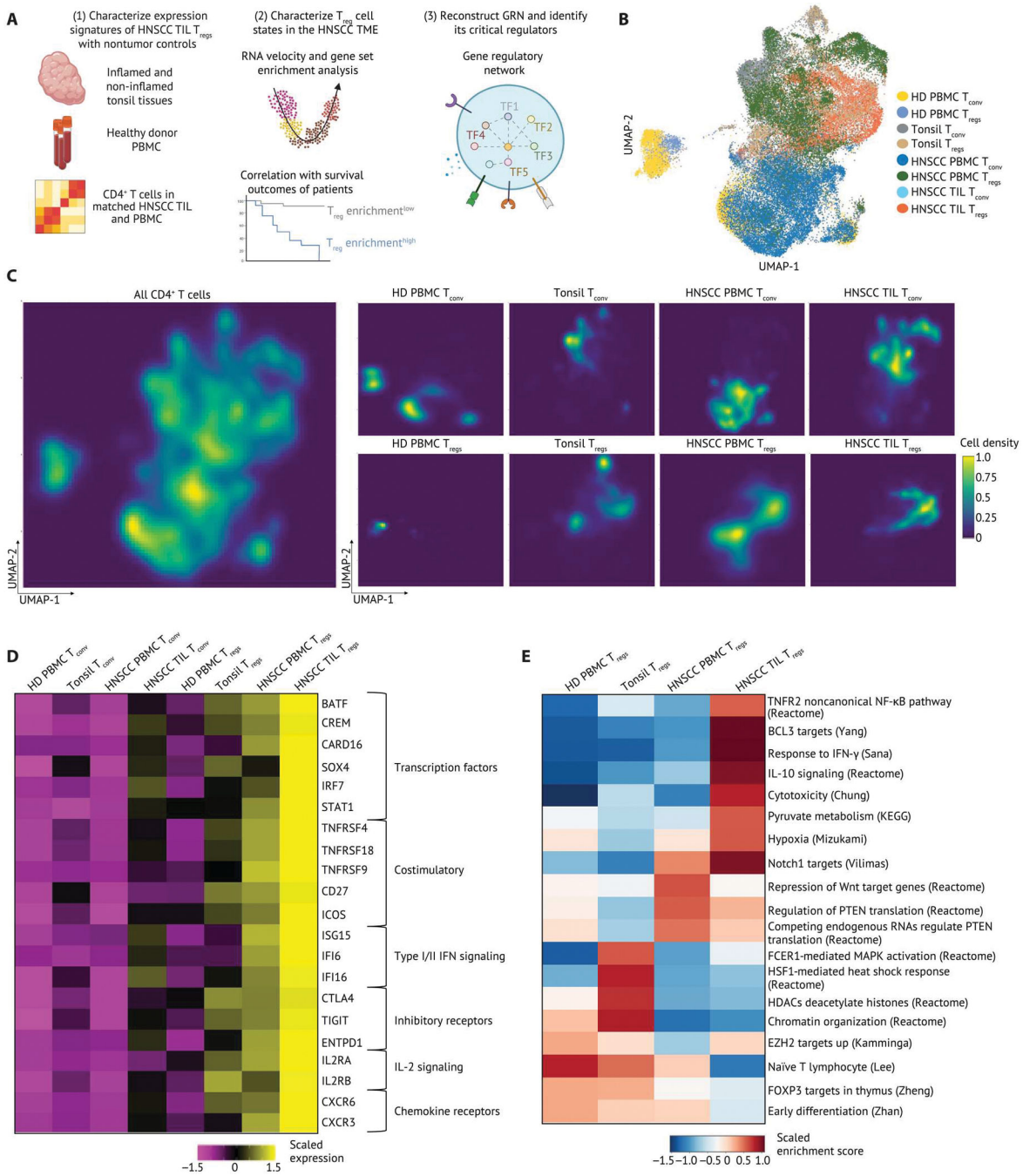

Fig. 1. Intratumoral CD4$^+$ T cells have distinct transcriptional signatures.

(**A**) Schematic of the experimental setup. Live T_{conv} and T_{regs} from HD blood and tonsil tissues were sequenced using 10X Genomics 3′ based scRNA-seq. scRNA-seq data were integrated with data from a previous study (19). We leveraged multiple bioinformatic approaches to identify cell types and states, infer drivers of differentiation, and reconstructed GRNs using SCENIC and causal MGM. (**B**) UMAP embedding and clustering of 51,195 CD4$^+$ T cells from matched TILs and PBMCs from patients with HNSCC (n = 26), tonsil tissues from patients with tonsilitis (n = 5), tonsil tissues from patients with sleep apnea

(n = 6), and HD PBMCs (n = 10). UMAP embedding of 51,195 $CD4^+$ T cells were color-coded by cell type and cell origin. (**C**) Two-dimensional galaxy plots of $CD4^+$ T cells were grouped by cell origins, and lighter color is indicative of a higher density of cells across sample groups. (**D**) A heatmap of gene signatures differentially expressed in HNSCC TIL T_{regs} compared with all other cells. The expression is scaled by transforming the gene expression in each population to zero mean, and unit SD is shown in the heatmap. (**E**) Selected gene sets that were highly enriched in subsets of T_{regs} were visualized on a heatmap. T_{regs} were grouped on the basis of the cell origin. The z-score of gene sets in each T_{reg} subset was calculated by R package Singleseqgset. Similarly, the enrichment score is scaled by row. KEGG, Kyoto Encyclopedia of Genes and Genomes. PTEN, phosphatase and tensin homolog.

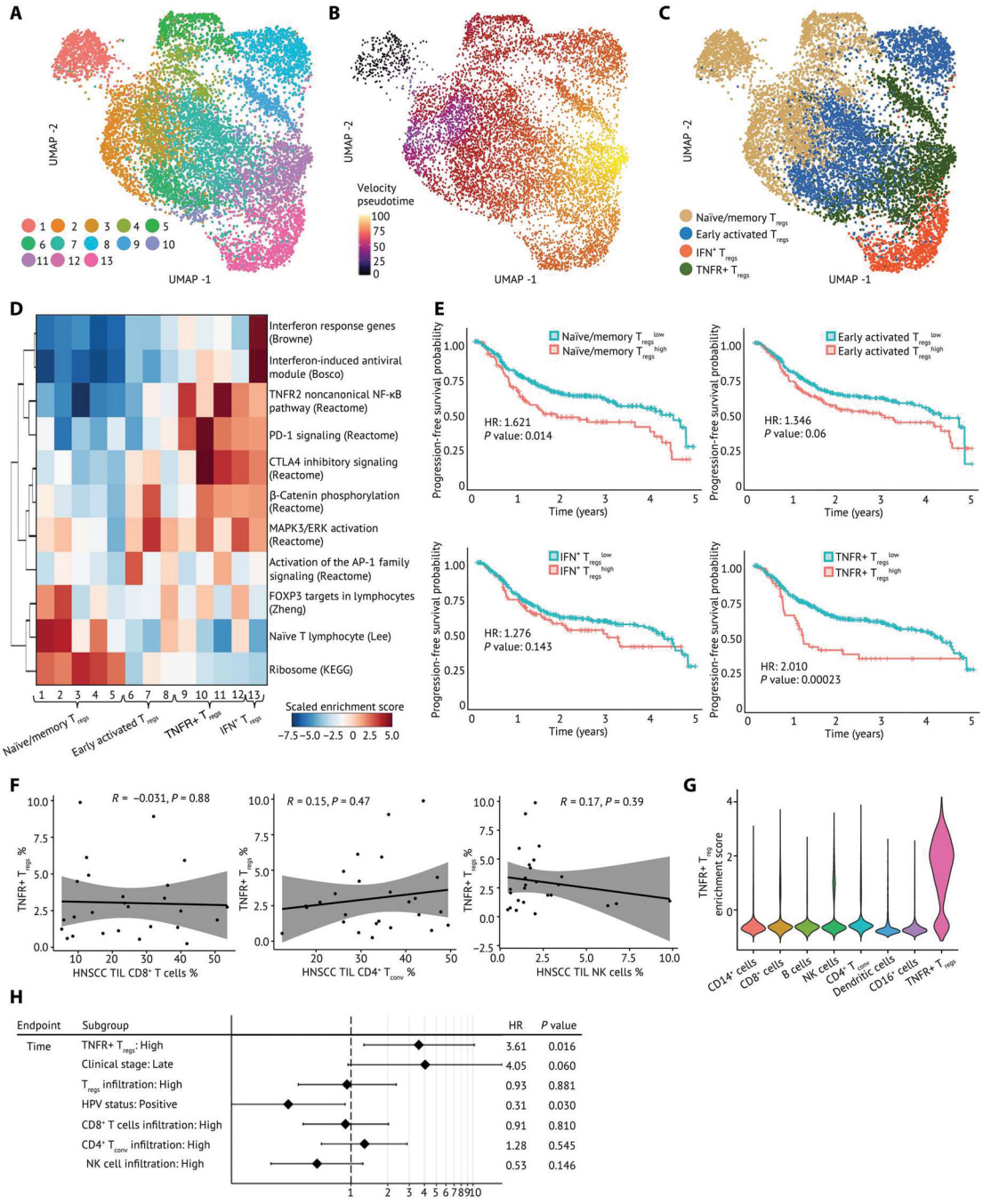

Fig. 2. Intratumoral T_{regs} are heterogeneous in the HNSCC TME and regulated by distinct transcriptional programs.

(**A**) A UMAP embedding of 9688 T_{regs} across all samples. Thirteen clusters were identified by Louvian graph–based unbiased clustering. (**B**) Pseudotime was derived from RNA velocity and visualized on a UMAP embedding, which revealed a differentiation process across T_{reg} clusters. (**C**) T_{regs} were annotated by cell state and visualized in a UMAP embedding. (**D**) Gene set enrichment analysis across T_{reg} clusters identified distinct phenotypes of T_{regs}. Specifically, clusters 1 to 5 are associated with naïve/memory T_{reg}

phenotype, clusters 6 to 8 have an early activated T_{reg} phenotype, clusters 9 to 13 exhibit an activated T_{reg} phenotype, clusters 9 to 12 are enriched for TNFR member genes, and cluster 13 has IFN response genes and a T_H1-like expression signature. The enrichment score is scaled by row. (**E**) Association of the enrichment of each T_{reg} subpopulation with survival outcomes of patients with HNSCC was calculated and visualized on Kaplan-Meier curves. Hazard ratio (HR) is calculated by monovariate Cox proportional regression, and the *P* value is calculated by likelihood ratio test. (**F**) Scatterplots of correlation between the frequency of $TNFR^+$ T_{regs} and $CD8^+$ T cells, $CD4^+$ T_{conv}, and NK cells. Pearson correlation coefficient (*R*) and *P* values (*P*) are calculated between $TNFR^+$ T_{regs} and each cell type. The proportion of each type among all lymphocytes in the HNSCC TME is shown. (**G**) Violin plot of the $TNFR^+$ T_{reg} signature in other cell types in the HNSCC TME. (**H**) Multivariable analysis of the enrichment of $TNFR^+$ T_{regs} and PFS outcomes.

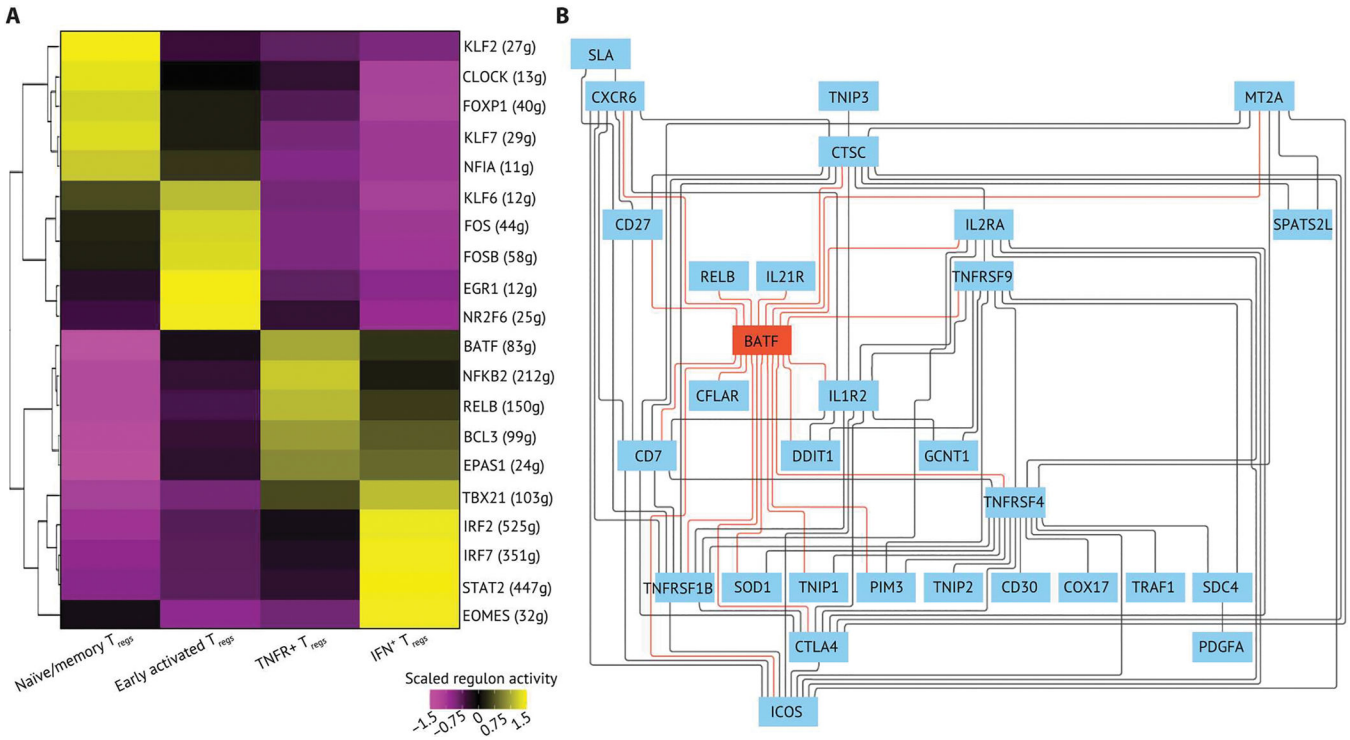

Fig. 3. An integrated BATF transcriptional network regulates key phenotypes of TNFR$^+$ T$_{regs}$.

(**A**) The top five regulons differentially expressed in each T$_{reg}$ state were ranked by log$_2$ fold change and visualized on a heatmap. The regulons were generated by using SCENIC with all T$_{regs}$ (*n* = 9736) in the dataset. The regulon score was calculated by using AUCell in R, and the regulon score of each T$_{reg}$ subpopulation is scaled by row. The top five regulons were determined by their log$_2$ fold change. (**B**) The GRN of TNFR$^+$ T$_{regs}$. The GRN was constructed using directed MGM and FCI-MAX modeling with TFs and downstream targets from the top five regulons in TNFR$^+$ T$_{regs}$. The direct connections between BATF and target genes are colored in red.

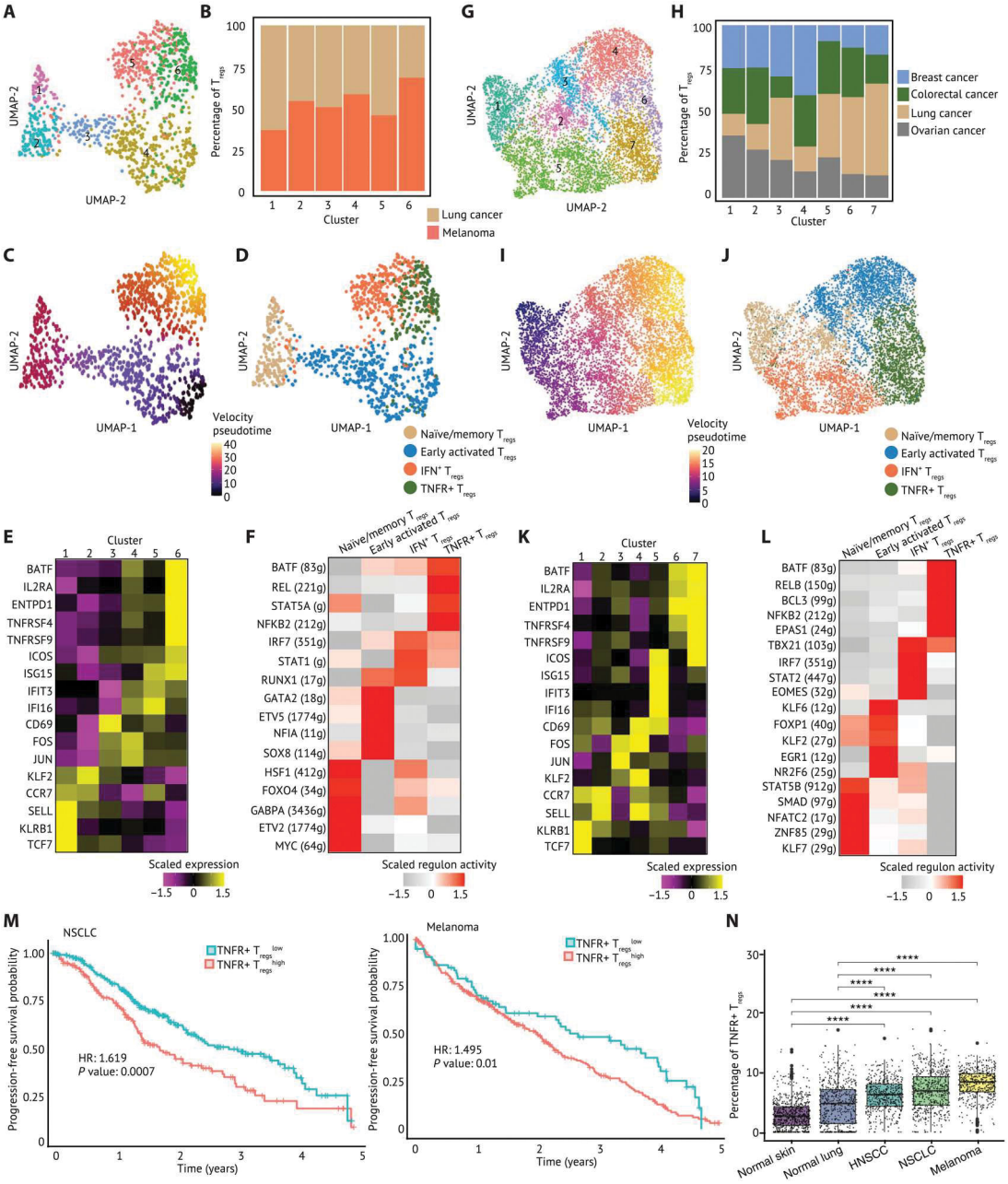

Fig. 4. TNFRSF-activated T_{regs} are highly enriched in solid TME compared with nontumor tissues and associated with worse prognosis across solid tumors.

(**A**) A UMAP embedding of 1294 T_{regs} in TILs and PBMCs from patients with melanoma (n = 4), NSCLC (n = 4), and SCLC (n = 1). Six clusters were identified by Louvian graph–based unbiased clustering. (**B**) A stacked barplot of percentage of T_{regs} in each cluster showed that T_{regs} from lung cancer and melanoma were distributed across six clusters. (**C**) Pseudotime derived from RNA velocity was visualized in a UMAP embedding, suggesting that T_{regs} in cluster 6 were at later pseudotime and more terminally differentiated. (**D**) T_{regs} were annotated by cell state and visualized in a UMAP embedding based on the cell state–related canonical marker genes, gene sets, and pseudotime inference. (**E**) The relative

expression of selected canonical marker genes is visualized on a heatmap. (**F**) The top five regulons differentially expressed in each T_{reg} cluster ranked by log_2 fold change were visualized on a heatmap. (**G**) A UMAP embedding of 7045 T_{regs} in TIL from patients with ovarian cancer ($n = 5$), lung cancer ($n = 8$), breast cancer ($n = 14$), and colorectal cancer ($n = 7$). Seven clusters were identified by unbiased clustering. (**H**) A stacked barplot of percentage of T_{regs} in each cluster highlights the distribution of T_{regs} from each tumor type. Clusters 6 and 7 were mixed with T_{regs} across tumor types. (**I**) Pseudotime inferred by Slingshot was visualized in a UMAP embedding. (**J**) T_{regs} were annotated by cell state and visualized in a UMAP embedding. (**K**) The relative expression of selected canonical marker genes is visualized on a heatmap. (**L**) The top five regulons differentially expressed in each T_{reg} cluster ranked by log_2 fold change were visualized on a heatmap. The gene expression and enrichment score are scaled by transforming the expression or enrichment score in each population to zero mean, and unit SD is shown in the heatmap. (**M**) Associations of the enrichment of each T_{reg} subpopulation with survival outcomes of patients with NSCLC and melanoma were calculated and visualized on Kaplan-Meier curves. Hazard ratio is calculated by monovariate Cox proportional hazard regression, and the P value is calculated by likelihood ratio test. (**N**) The enrichment of $TNFR^+$ T_{regs} visualized in box plots was inferred using Cibersortx on datasets from the TCGA and GTEx. The inferred proportion of $TNFR^+$ T_{regs} among all cells within each tissue score is shown. A pairwise comparison between each tissue source is calculated by a nonparametric Wilcoxon signed rank test. P values: ****$P \leq 0.0001$.

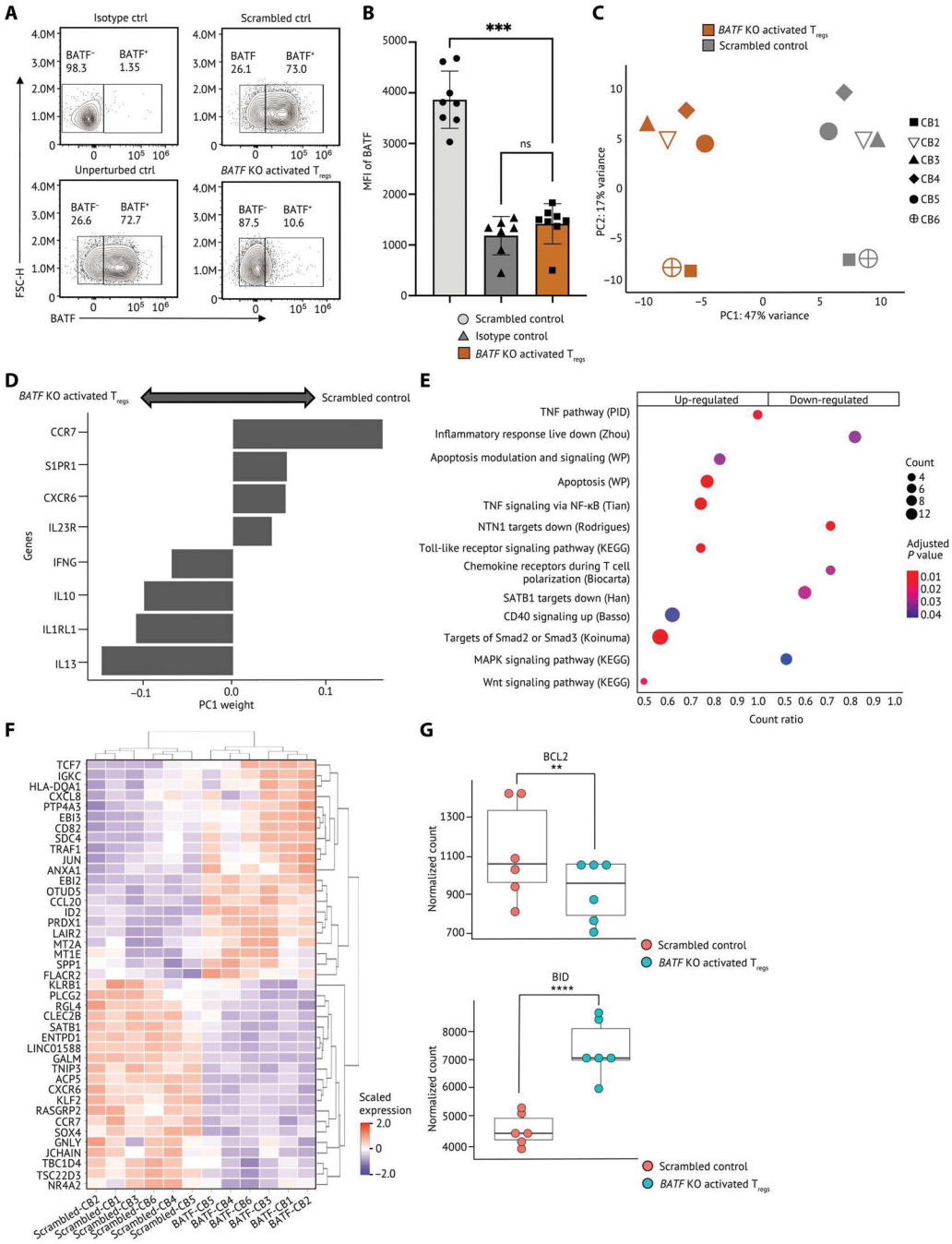

Fig. 5. CRISPR/Cas9-RNP KO reveals that BATF regulates human activated T_{regs} by multiple signaling pathways.

(**A** and **B**) Human primary T_{regs} isolated from cord blood were CRISPR-edited and then cultured with TCR stimulation for 3 days. (A) Representative flow staining of T_{regs} showing BATF protein level in nontargeting scrambled control and unperturbed control T_{regs}. (B) The BATF expression by median fluorescence intensity (MFI) in T_{regs} ($n = 8$) is shown. Each dot indicates an individual replicate. Bars indicate the median of expression, and error bars represent 1 SD. (**C** to **G**) RNA-seq was conducted on *BATF* KO activated T_{regs} (*n*

= 6) and scrambled control from the same donor. (C) PCA of the transcriptome of the scrambled control and *BATF* KO activated T_{regs}. Human activated T_{regs} were stratified by PC1. (D) Weightings of the genes that were the strongest drivers of PC1 were visualized on a bar plot. (E) Selected gene sets that were enriched in human *BATF* KO activated T_{regs} were visualized on a dot plot. Genes are differentially expressed in both $TNFR^+$ T_{regs} from scRNA-seq and *BATF* KO activated T_{regs} in bulk RNA-seq selected as input to the gene set enrichment analysis. Dots are colored by the false discovery rate (FDR)–adjusted *P* value, and dot sizes are scaled by the number of significantly up-regulated genes within each gene set (<0.1% FDR). (F) The relative expression of the top 20 up/down-regulated genes differentially expressed in both $TNFR^+$ T_{regs} and *BATF* KO activated T_{regs} were visualized on a heatmap. The gene expression is scaled by row. (G) Dot plots showing the expression levels of *BCL2* and *BID* in *BATF* KO activated T_{regs} and scrambled controls from eight individual replicates. Data in (B) were analyzed by a ratio paired *t* test, and the FDR *P* values in (G) were calculated by Wald test. *P* values: $^{**}P < 0.01$; $^{***}P < 0.001$, $^{****}P < 0.0001$. ns, not significant.

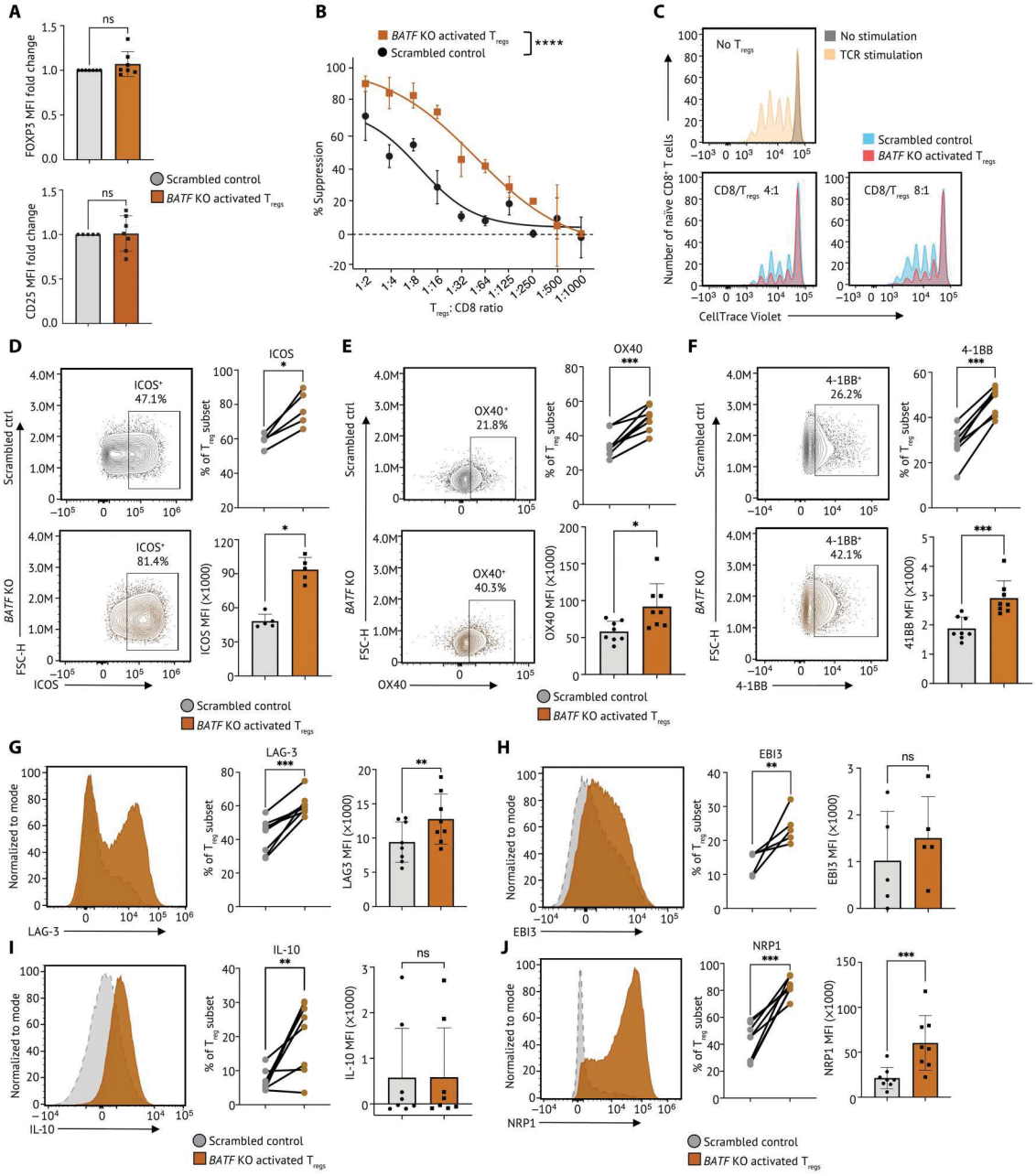

Fig. 6. BATF modulates the suppressive function of human activated T_{regs}.

(**A**) Tabulation of FOXP3 (top) and CD25 expression (bottom) in *BATF* KO activated T_{regs} ($n = 7$) and scrambled control from the same donor. Data were reported as fold change normalized to marker MFI of nontargeting scrambled control groups. Each dot indicates an individual replicate. Bars indicate the median of expression, and error bars represent 1 SD. (**B**) In vitro microsuppression assay comparing *BATF* KO activated T_{regs} ($n = 6$) and scrambled control from the same donor are shown. (**C**) Representative $CD8^+$ T cell proliferation in Fig. 6B at different conditions: no TCR stimulation (gray); 5-day TCR stimulation without coculture with T_{regs} (yellow); 5-day TCR stimulation with CD8:T_{reg} ratios as 4:1 and 8:1. Cell number at each condition was normalized to the highest cell

number in the plot. (**D**) The expression of ICOS on *BATF* KO activated T_{regs} and scrambled control were determined by flow cytometry. The percentage of T_{regs} expressing ICOS was summarized on a dot plot, and the MFI of ICOS on T_{regs} was summarized on a bar plot. Data were pooled from five individual replicates. (**E**) The expression of OX40 on *BATF* KO activated T_{regs} and scrambled control were visualized by represented flow cytometry plots from eight individual replicates. The percentage of T_{regs} expressing OX40 was summarized on a dot plot, and the MFI of OX40 on T_{regs} ($n = 8$) was summarized on a bar plot. (**F**) The expression of 4–1BB on *BATF* KO T_{regs} and scrambled control were visualized by represented flow cytometry plots from seven individual replicates. The percentage of T_{regs} expressing 4–1BB was summarized on a dot plot, and the MFI of 4–1BB in T_{regs} was summarized on a bar plot. (**G** to **J**) The expression of (G) LAG-3, (H) EBI3, (I) IL-10, and (J) NRP1 on *BATF* KO activated T_{regs} and scrambled control were visualized by represented flow cytometry plots from five individual replicates. The percentage of T_{regs} expressing marker genes and the MFI were summarized on a dot plot and a bar plot, respectively. Samples from the same donor were connected by solid lines. Each dot indicates an individual replicate. Bars indicate the median of expression, and error bars represent 1 SD. Data were pooled from five to eight individual replicates. Markers that have fewer replicates than others were subsequently incorporated into the flow panel as the study progressed. Data in (A) and (D) to (J) were analyzed by a ratio paired *t* test, and data in (B) were analyzed by two-way ANOVA test. *P* values: ns: $P > 0.05$; *$P \leq 0.05$; **$P \leq 0.01$; ***$P \leq 0.001$, ****$P \leq 0.0001$.

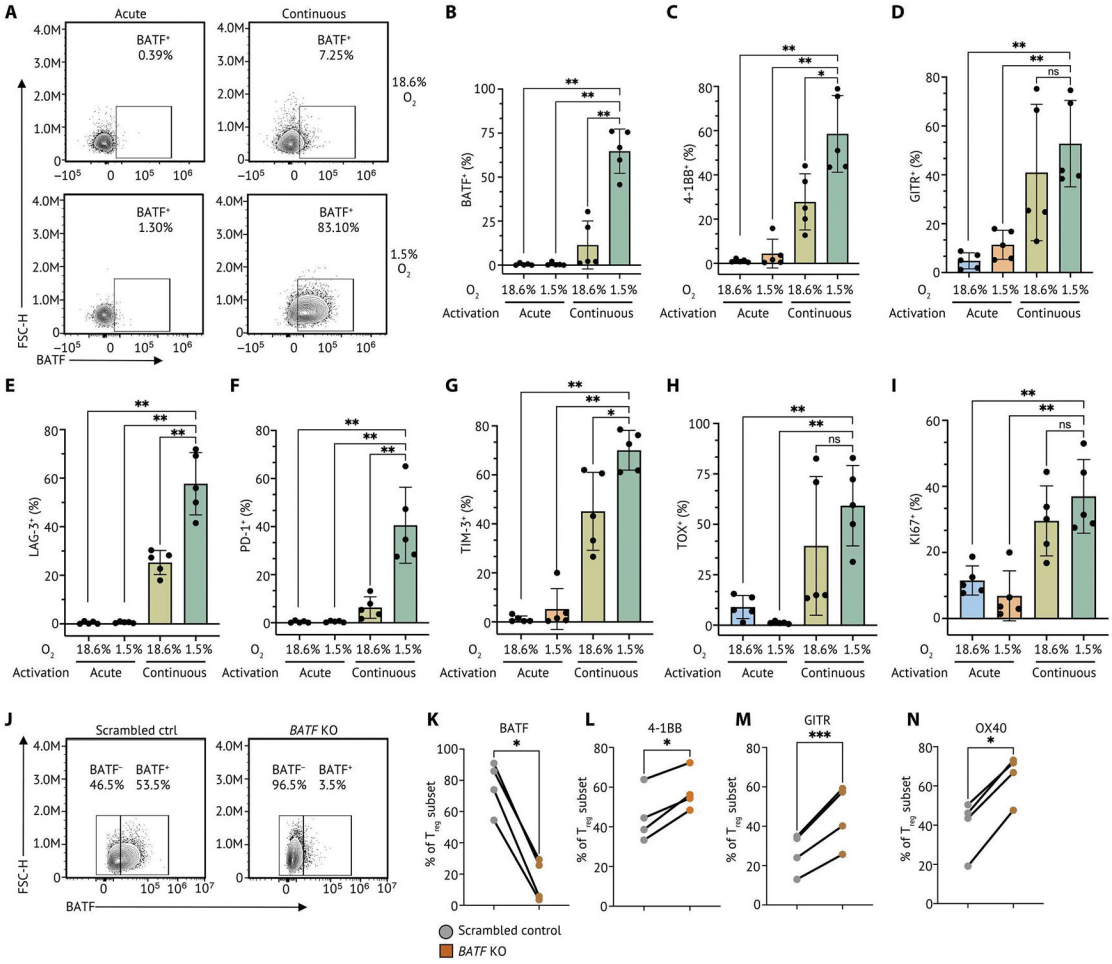

Fig. 7. Human T_{regs} cultured with continuous TCR stimulation under hypoxia mimic intratumoral BATF-driven TNFR+ T_{reg} phenotypes.

(**A**) Human primary T_{regs} isolated from cord blood were cultured in acute TCR stimulation (acute) in normoxia (20% O_2), continuous TCR stimulation (continuous) in normoxia, acute stimulation in hypoxia (1.5% O_2), and continuous stimulation in hypoxia. Representative flow cytometry plots of five individual replicates showing BATF protein level in T_{regs} with continuous TCR stimulation under normoxia and hypoxia. (**B**) A bar plot summarizing the percentage of T_{regs} expressing BATF identified in T_{regs} in each culture condition. The percentage of T_{regs} expressing 4–1BB (**C**), GITR (**D**), LAG-3 (**E**), PD-1 (**F**), TIM-3 (**G**), TOX (**H**), and KI67 (**I**) identified in $TNFR^+$ T_{regs} ($n = 5$) was summarized on a bar plot. Each dot indicates an individual replicate. Bars indicate the median of expression, and error bars represent 1 SD. (**J**) *BATF* deletion was conducted by CRISPR RNP KO in human T_{regs} with continuous TCR stimulation under hypoxia at day 10. Representative flow cytometry plots of four individual replicates showing the proportion of T_{regs} expressing BATF after 48-hour repeated TCR stimulation. (**K**) Tabulation of the percentage of T_{regs} expressing BATF from four individual replicates. (**L** to **N**) The percentage of T_{regs} expressing 4–1BB, GITR, and OX40 was summarized on a dot plot. Samples from the same donor were connected by solid lines, and each dot indicates an individual replicate. Data were pooled from four individual replicates. Data in (B) to (I) were analyzed by a nonparametric Mann-Whitney *U*

test, and data in (K) to (N) were analyzed by a ratio paired *t* test. *P* values: ns: $P > 0.05$; *$P < 0.05$; **$P < 0.01$; ***$P < 0.001$.

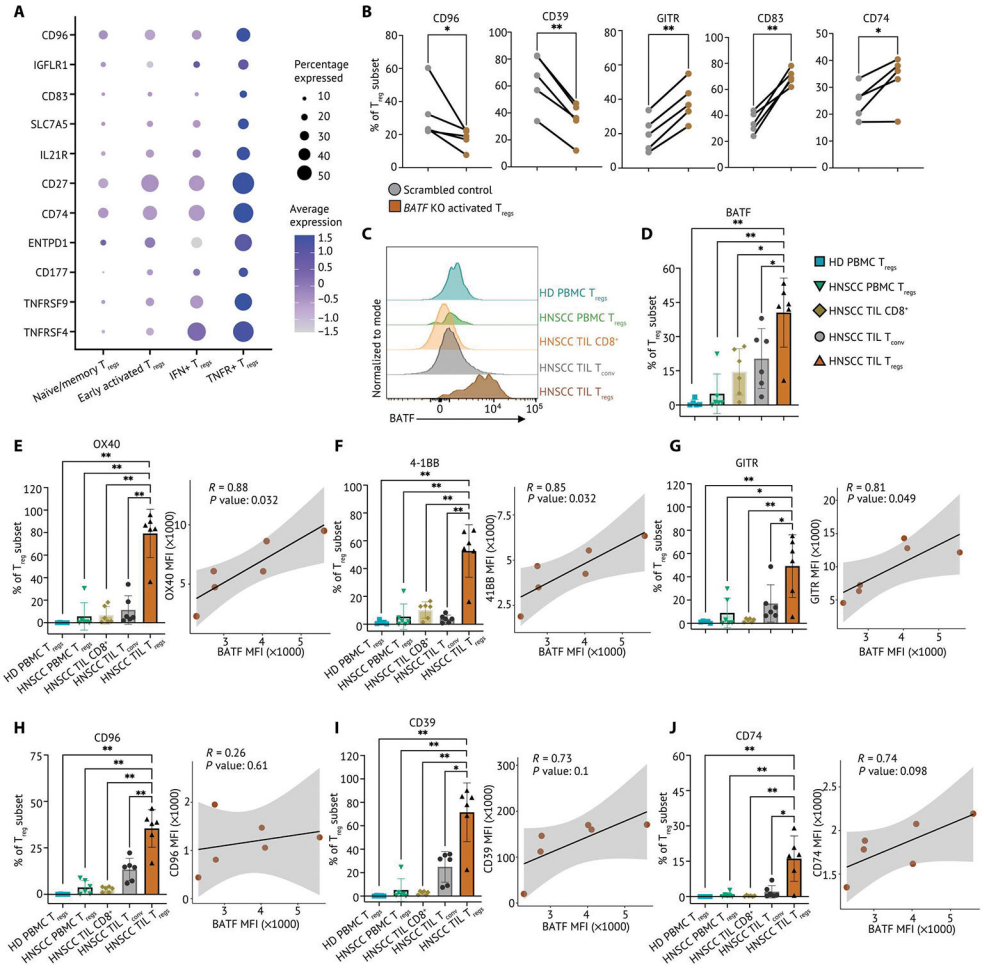

Fig. 8. TNFR$^+$ T$_{regs}$ express BATF-regulated surface markers preferentially in the HNSCC TME.

(**A**) Relative expression of surface markers differentially expressed on TNFR$^+$ T$_{regs}$ and percentage of T$_{reg}$ subset in the single-cell HNSCC dataset were visualized on a dot plot. (**B**) Frequency of CD96, CD39, GITR, CD83, and CD74 expression determined by flow cytometry from control and *BATF-null* human activated T$_{regs}$ from cord blood (n = 5). Samples from the same donor were connected by solid lines, and each dot indicates an individual replicate. (**C**) Matched TILs and PBMCs from patients with HNSCC (n = 6) and HD PBMC (n = 5) were stained for flow cytometry phenotyping. Representative flow plot of BATF expression in TILs and PBMCs from patients with HNSCC and HD PBMCs, normalized to mode scales as a percentage of the maximum count. (**D**) Tabular summary of percentage of cells expressing BATF from patients with HNSCC (n = 6) and HD PBMCs (n = 5). (**E** to **J**) The percentage of T$_{regs}$ expressing surface markers identified in TNFR$^+$ T$_{regs}$ from matched TILs and PBMCs from patients with HNSCC (n = 6) and HD PBMCs (n = 5) is summarized on a bar plot. Each dot indicates an individual replicate. Bars indicate the median of expression, and error bars represent 1 SD. The coexpression of BATF expression and marker genes by MFI in HNSCC TIL T$_{regs}$ was shown in scatterplots. The Pearson correlation coefficient (R) between the expression BATF and marker genes was calculated by the MFI in HNSCC TIL T$_{regs}$. The significance of Pearson correlation coefficient (P) was

calculated by *t* test. Data in (B) were analyzed by a ratio paired *t* test, and data in (D) to (J) were analyzed by a nonparametric Mann-Whitney *U* test. *P* values: *$P \leq 0.05$; **$P \leq 0.01$.